

Epigenetic modulation via the C-terminal tail of H2A.Z

Received: 8 July 2022

Accepted: 12 October 2024

Published online: 24 October 2024

 Check for updates

László Imre¹, Péter Nánási Jr¹, Ibtissem Benhamza¹, Kata Nóra Enyedi^{2,3}, Gábor Mocsár⁴, Rosevalentine Bosire¹, Éva Hegedűs¹, Erfaneh Firouzi Niaki¹, Ágota Csóti¹, Zsuzsanna Darula^{5,6}, Éva Csősz⁷, Szilárd Póliska⁷, Beáta Scholtz⁷, Gábor Mező^{2,3}, Zsolt Bacsó¹, H. T. Marc Timmers⁸, Masayuki Kusakabe⁹, Margit Balázs¹⁰, György Vámosi¹, Juan Ausio¹¹, Peter Cheung¹², Katalin Tóth¹, David Tremethick¹³, Masahiko Harata¹⁴ & Gábor Szabó¹✉

H2A.Z-nucleosomes are present in both euchromatin and heterochromatin and it has proven difficult to interpret their disparate roles in the context of their stability features. Using an in situ assay of nucleosome stability and DT40 cells expressing engineered forms of the histone variant we show that native H2A.Z, but not C-terminally truncated H2A.Z (H2A.ZΔC), is released from nucleosomes of peripheral heterochromatin at unusually high salt concentrations. H2A.Z and H3K9me3 landscapes are reorganized in H2A.ZΔC-nuclei and overall sensitivity of chromatin to nucleases is increased. These tail-dependent differences are recapitulated upon treatment of HeLa nuclei with the H2A.Z-tail-peptide (C9), with MNase sensitivity being increased genome-wide. Fluorescence correlation spectroscopy revealed C9 binding to reconstituted nucleosomes. When introduced into live cells, C9 elicited chromatin reorganization, overall nucleosome destabilization and changes in gene expression. Thus, H2A.Z-nucleosomes influence global chromatin architecture in a tail-dependent manner, what can be modulated by introducing the tail-peptide into live cells.

The variant histone H2A.Z is involved in the regulation of diverse and basic cell functions, with activating as well as repressive effects that have proved difficult to reconcile with the structural information available for the nucleosomes containing H2A.Z. It contributes to the

regulation of transcriptional initiation and elongation, DNA replication, heterochromatin organization, DNA repair, cell differentiation and cell cycle, and epithelial mesenchymal transition in embryonic development. It is also upregulated in a variety of different types of

¹Department of Biophysics and Cell Biology, Faculty of Medicine, University of Debrecen, Debrecen, Hungary. ²Department of Organic Chemistry, Institute of Chemistry, Eötvös Loránd University, Budapest, Hungary. ³HUN-REN-ELTE, Supported Research Groups, Research Group of Peptide Chemistry, Budapest, Hungary. ⁴Damjanovich Cell Analysis Core Facility, Department of Biophysics and Cell Biology, University of Debrecen, Faculty of Medicine, Debrecen, Hungary. ⁵Single Cell Omics Advanced Core Facility, Hungarian Centre of Excellence for Molecular Medicine, Szeged, Hungary. ⁶Core Facility, Proteomics Research Group, HUN-REN Biological Research Centre, Szeged, Hungary. ⁷Department of Biochemistry and Molecular Biology, Faculty of Medicine, University of Debrecen, Debrecen H-4032, Hungary. ⁸German Cancer Consortium (DKTK), partner site Freiburg, a partnership between the DKFZ and Medical Center-University of Freiburg and Department of Urology, Medical Center-University of Freiburg, Breisacher Str. 66, Freiburg, Germany. ⁹Biosignal Research Center, Kobe University, 1-1 Rokkodai-cho, Nada-ku, Kobe 657-8501, Japan. ¹⁰HUN-REN-UD Public Health Research Group, Department of Public Health and Epidemiology, Faculty of Medicine, University of Debrecen, Debrecen, Hungary. ¹¹Department of Biochemistry and Microbiology, University of Victoria, Victoria, British Columbia, Canada. ¹²York University, Toronto, Canada. ¹³The John Curtin School of Medical Research, The Australian National University, Canberra, ACT 2601, Australia. ¹⁴Laboratory of Molecular Biology, Graduate School of Agricultural Science, Tohoku University, Sendai, Japan. ✉e-mail: szabog@med.unideb.hu

cancers, has important roles in intestinal epithelial cell homeostasis, Wnt, Notch, Nanog, Gli1 signaling, and in central nervous system development and function (for reviews see^{1,2}). H2A.Z exhibits about 60% identity to canonical H2A and constitutes approximately 5% of the total H2A histone pool in vertebrates³.

Since the nucleosomal structure is, in general, repressive for transcription, replication and repair, one strategy of eukaryotic cells to regulate these activities involves de-repression by destabilizing or mobilizing particular nucleosomes. As such, the stability of nucleosomes is of utmost regulatory importance, and it can be modulated by posttranslational modifications (PTMs) on histones, the reader proteins binding to them as well as by histone variant composition⁴. In this context, destabilizing effects are expected in the case of activating functions, while nucleosome stabilization would suit repressive roles. In a puzzling manner, there are observations suggesting that the presence of H2A.Z in nucleosomes can increase^{5–11}, or decrease^{6,12–19} nucleosome stability, which underscore the context-dependent complexity of this variant^{20,21}. Even similar experimental approaches have led to disparate conclusions, such as the different findings from Förster resonance energy transfer measurements on reconstituted nucleosomes^{5,20} or magnetic tweezer unzipping measurements^{11,15}. On the other hand, in genomics studies, destabilizing effects are regularly described. For example, the presence of H2A.Z destabilizes local nucleosome structure in ES cells, leading to decreased nucleosome occupancy and increased chromatin accessibility, particularly at enhancers¹⁶. In line with this report, H2A.Z deposition creates wide ATAC-Seq positive promoter regions in *mouse* fibroblasts genome-wide¹⁸. Furthermore, decreased unwrapping of the +1 nucleosomes has been found recently by MNase-X-ChIP-seq upon depletion of H2A.Z¹⁹. Unusually labile (i.e., sensitive to low concentration of NaCl) H2A.Z-containing nucleosomes have been detected at the TSS (transcription start site) region of transcriptionally active promoters¹⁴, particularly those flanking nucleosome-free regions at TSSs that contain H2A.Z paired with the H3.3 variant²². Context-dependent variation of H2A.Z nucleosome stability has been demonstrated by a differential MNase digestion approach revealing that H2A.Z nucleosomes upstream or downstream of the TSS are much more resistant to MNase than those at the TSS²³. One possible explanation for some of the above differences is how nucleosome stability is defined and measured. On the other hand, since H2A.Z-containing nucleosomes are also present in the transcriptionally repressed heterochromatin^{24,25} with stability features likely different from those of the euchromatic localization, the different results may also be related to the possible intranuclear heterogeneity of H2A.Z nucleosomes.

In *human* cells, H2A.Z is loaded onto chromatin by the Tip60/p400 and SRCAP chromatin remodeling complexes, while ANP32E and INO80 are responsible for its eviction. In addition to the INO80 type remodelers, ISWI and CHD family protein complexes have also been implicated in the replication-independent dynamics of the variant (for review see ref. 26). These activities must be superimposed on and also influence, the nucleosome-autonomous stability features.

H2A.Z has two isoforms, H2A.Z.1 and H2A.Z.2.1, which differ in only 3 amino acids²⁷ and are encoded by separate genes. The two isotypes have indispensable and selective functions during development^{28,29} and appear to have distinct roles in controlling normal and cancer cell proliferation^{30,31}. Only subtle structural differences between canonical and H2A.Z-containing nucleosomes were revealed by X-ray crystallography^{32,33}. Alternative splicing gives rise to the hypervariant H2A.Z.2.2 that is shorter than H2A.Z.1 or Z2 by 14 amino acids and markedly destabilizes nucleosomes relative to H2A.Z.1 or H2A³³. Through the spectacles of mobility features of nucleosomal DNA termini, cryo-EM studies²¹ support the notion of a destabilizing role of H2A.Z which depends on its C-terminal tail; however, the same study has also demonstrated the formation of more condensed chromatin fibers in the presence of H2A.Z (recently reviewed in ref. 34). In a

recent high-speed atomic microscopic (AFM) study³⁵, interaction between the N-terminal region of H2A.Z.1 and the DNA was found to be responsible for nucleosome sliding, at variance with²¹. In summary, the different approaches addressing the relationships between the stability features of H2A.Z-containing nucleosomes and their other characteristics, including isoform composition, post-translational modifications (PTMs) and their roles in euchromatin vs. heterochromatin, have not yet led to a fully coherent picture^{2,30}.

In this work, we made use of an *in situ* assay of nucleosome stability, QINESIn (Quantitative Imaging of Nuclei after Elution with Salt/Intercalators)³⁶ to gain insights into the stability features of H2A.Z-containing nucleosomes in close to native conditions of chromatin. This quantitative imaging cytometry-based assay delivers histone type, PTM- and cell cycle phase-specific information on the stability features of nucleosomes consisting of native endogenous or ectopically expressed histones, in populations of individual nuclei. A unique genetic complementation system³⁷ was also employed, involving H2A.Z.1 and Z2 double knock out (DKO) DT40 cell lines expressing transduced H2A.Z.1, Z2, a non-acetylable Z1 mutant or a truncated H2A.Z.1 missing its C-terminal 9 amino acids^{27,37,38}, to learn what role the related factors may have in determining nucleosome stability *in vivo*. Having observed remarkable changes of nucleosome stability, nuclear architecture and accessibility features of chromatin in the case of the C-terminal deletion, the effect of a peptide representing the tail (C9) on these features was tested in permeabilized nuclei, and its binding to reconstituted nucleosomes was studied by fluorescence correlation spectroscopy (FCS). Based on these observations and the effect of C9 introduced into live cells on gene expression, a central role of the alternative engagements of the C-terminal H2A.Z tail in the functioning of this histone variant emerges and the possibility of epigenetic modulation via introducing C9 into live cells is demonstrated.

Results

H2A.Z-containing nucleosomes exhibit intranuclear heterogeneity regarding their stability features and intranuclear localization

Using QINESIn (Suppl. Fig. 1A, B), we show that H2A.Z can be unusually stably chromatin associated (Fig. 1A), exhibiting salt elution profiles typical of H3 or H4 (see ref. 36, and refs. cited therein), as compared to canonical H2A or H2A.X, in every phase of the cell cycle (Fig. 1B). In QINESIn, the curves represent the average immunofluorescence (IF) of agarose-embedded nuclei left behind after their treatment with the indicated concentration of salt. The apparent stability of the H2A.Z-containing nucleosomes depends on which anti-H2A.Z antibody is applied to visualize the histone variant: an Abcam antibody (generated against the C-terminus of the histone starting with amino acid 65, comprising the H2A.Z docking domain and the C-terminal unstructured tail; see Suppl. Fig. 1C; designated ZAbA from here on) and three others (Suppl. Fig. 2A–D) detect the stable H2A.Z-containing nucleosomes, while the Thermo Fisher Scientific antibody PA5-17336 (generated against a peptide sequence surrounding amino acid residue 118 of the docking domain, near the tail; designated ZAbB) detects H2A.Z in nucleosomes behaving similarly to those containing the canonical H2A (see dashed line in Fig. 1C), or to fluorescent protein-tagged H2A.Z (see below). (Since all the antibodies used detect both isoforms, the isoform-specific designations of the histone will be used in the text only when H2A.Z.1 and H2A.Z.2.1 could be distinguished.) Different antibodies detect H2A.Z at different nuclear localizations: ZAbA recognizes H2A.Z nucleosomes mainly at the nuclear periphery, while ZAbB staining gives a more scattered pattern (Fig. 1D, E). Suppl. Fig. 2E demonstrates that the H3-like stability of H2A.Z approached the H2A-like features when the nuclei were pretreated with a frequent-cutter nickase; we have previously shown that topological relaxation via nicking destabilizes nucleosomes to salt such that eviction of the dimers is facilitated³⁶. Thus, the same antibody is able to identify H2A.Z

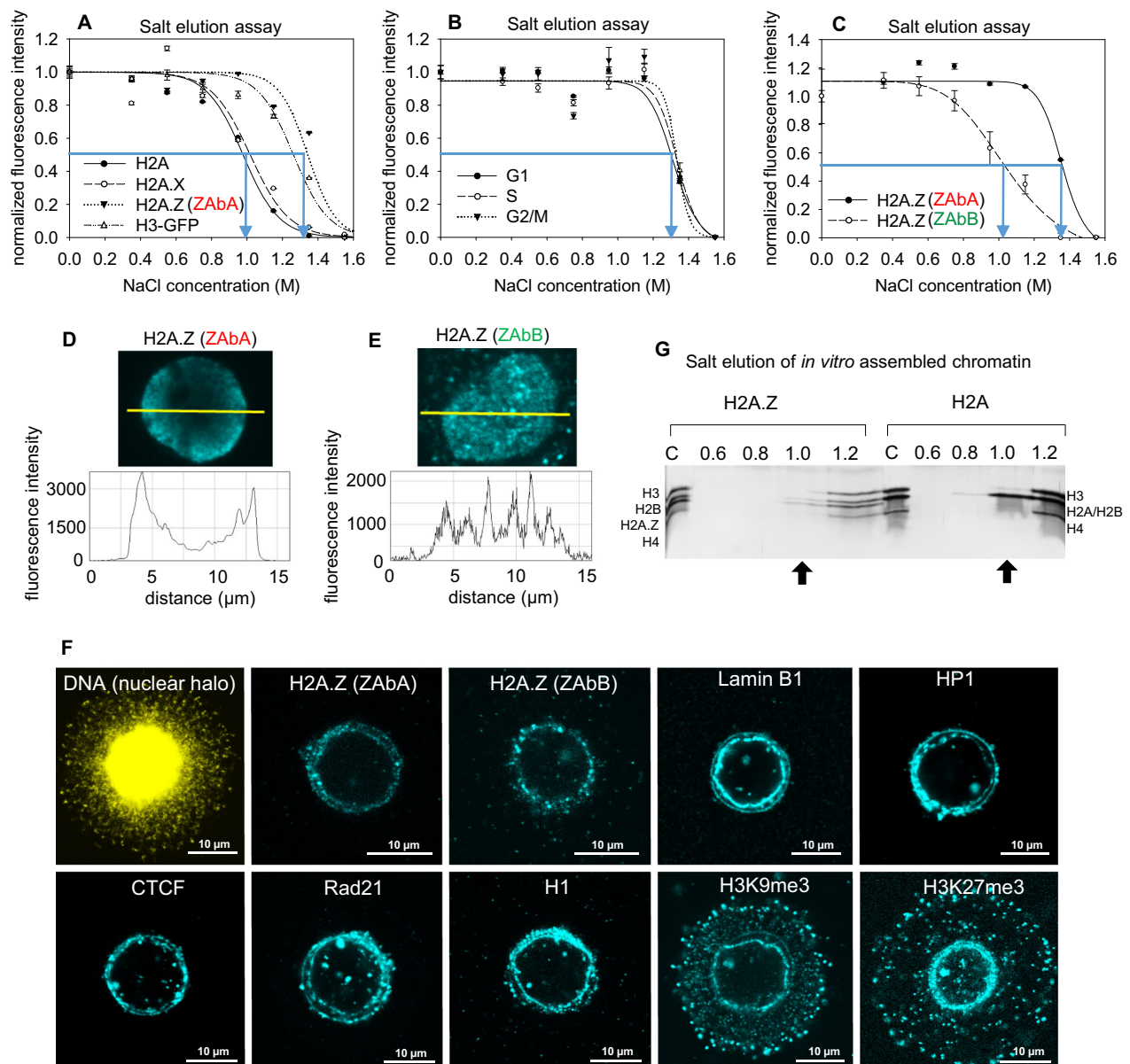


Fig. 1 | Intranuclear heterogeneity of H2A.Z. **A** Comparison of the salt elution profiles, measured by QINESIn (as in Suppl. Fig. 1A), of H2A, H2A.X, H2A.Z (detected by the antibody ZAbA; Abcam, ab 97966) and of H3-GFP (used as an internal control) in HeLa nuclei. **B** Salt elution profile of H2A.Z detected by ZAbA in HeLa nuclei of different cell cycle phases. **C** Salt elution curves of H2A.Z detected by ZAbB (Thermo Fisher Sci.) and ZAbA, measured separately in HeLa nuclei. In (A–C), the elution curves refer to G1 phase nuclei gated according to their DNA fluorescence intensity distribution and the error bars represent SEM of ~600 nuclei measured by LSC. Blue arrows on the elution curves indicate EC50 values (also in the other

figures). **D, E** CLSM images and line-scans showing nuclear localization of H2A.Z as recognized by ZAbA (**D**), or by ZAbB (**E**). **F** IF staining of H2A.Z (using ZAbA or ZAbB), Lamin B1, HP1, CTCF, Rad21, H1, H3K9me3, and H3K27me3 in halo samples of HeLa nuclei. Representative images are shown. **G** Hydroxyapatite dissociation chromatography analyses of chromatin assembled *in vitro* using *Xenopus laevis* N1/N2- (H3, H4) and recombinant H2A/H2B or H2A.Z.1/H2B (see “Methods”). The H2A/H2B dimers run on the gel as a single band. See full gel image in Suppl. Fig. 3D. Arrows point at the histones eluted at 1 M salt.

within stable or unstable nucleosomes depending on the superhelical state of the DNA. Antibody labeling follows the salt elution step in QINESIn, so it cannot affect the elution characteristics of a histone.

H2A.Z isotype composition, PTMs that can mark H2A.Z, and the presence or absence of the C-terminus binding reader protein PWWP2A³⁸ could all affect the stability of nucleosomes containing H2A.Z. However, employing inhibitors and cell lines expressing different isoforms or mutants of H2A.Z in a double KO (DKO) DT40 background³⁷ we have shown that the stability features measured do not depend on H2A.Z isotype specificity, acetylation, ubiquitination or sumoylation (Suppl. Figs. 2G–L and 3A–C). The finding that the H2A.Z elution curves were similar at different PWWP2A expression

levels is not surprising in view of the fact that the reader is eluted at rather low salt, so it could not affect the stability features measured in our assay (see Suppl. Fig. 3C). Due to the same reason, the unusual stability features of H2A.Z as detected by ZAbA cannot be due to PWWP2 binding either. The above negative data are in line with published observations made on reconstituted nucleosomes confirmed in Fig. 1G (see also Suppl. Fig. 3D): A higher concentration of NaCl was required to elute H2A.Z as compared to H2A being co-eluted with histone H3, recapitulating the salt elution profile in HeLa cells (Fig. 1A–C), as analyzed by hydroxyapatite chromatography³⁹. These observations suggest that the unusual behavior of H2A.Z detected by several antibodies (Abcam 97966, 4174, 18262 and

Millipore 07-594) is an autonomous feature of certain nucleosomes containing the variant histone.

When the salt elution curves of Fig. 1A were plotted without normalization to zero endpoint (Suppl. Fig. 2F), a ~10% fraction of H2A.Z remained in the nuclei after the highest concentration of salt. This fraction was apparently bound to the nuclear lamina according to the confocal laser scanning microscopic (CLSM) images of nuclear halo samples, as shown in Fig. 1F. H2A.Z was present in two concentric layers of the lamina, recapitulating its superresolution structure⁴⁰. This fraction is referred to from here on as H2A.Z^{lmm}. Interestingly, beside H2A.Z, CTCF, H1, H3K9me3, H3K27me3, HPI, and the cohesin subunit Rad21 were also present in the two layers. Most of these proteins were also detected by mass spectrometric analyses of the halo samples (Suppl. Table 1).

Interestingly, the fluorescent protein-tagged forms of H2A.Z.1 and Z2 both show a destabilized character, similarly to what was observed through the spectacles of ZAbB, and this was invariant to the N- or C-terminal localization of the protein-tag (Suppl. Fig. 4A, B). As the co-labeling experiment of Suppl. Fig. 4C shows, the ZAbA-detected chromatin elements exhibit peripheral localization, while the tagged forms, similarly to the ZAbB-detected histones, are distributed in a scattered fashion in the nucleus, suggesting that ZAbA and ZAbB preferentially recognize different subsets of the variant in the nucleus. The intranuclear localization and stability features of H2A.Z-nucleosomes were both sensitive to even small tags, particularly when present at the C-terminus (Suppl. Fig. 4D–F). The specificity of the antibodies was demonstrated in Western blots using recombinant histones⁴¹ (see Suppl. Fig. 5A–C), and also confirmed in experiments where silencing of H2A.Z using shRNA²⁴ has led to decreased H2A.Z IF before cell death would occur (Suppl. Fig. 5D–G). H2A.Z silencing induced reorganization of the heterochromatin (Suppl. Fig. 5H, I), concomitant with the disappearance of the histone variant from the H3K9me3-rich peripheral heterochromatin (Suppl. Fig. 5G, H). Suppression of the binding of ZAbA by recombinant H2A.Z.1 protein was also demonstrated (Suppl. Fig. 5J). Silencing was confirmed also in western blots (Suppl. Fig. 6A–E) and by co-transfection of the silencing construct with a GFP-expressor plasmid allowing the separate gating of successfully transfected cells in the laser scanning cytometric (LSC) analysis of H2A.Z expression (Suppl. Fig. 6F–H).

Thus, two kinds of H2A.Z containing chromatin regions can be distinguished: ZAbA-detected salt-stable ones likely associated with the peripheral heterochromatin (designated H2A.Z^{hc}; see Fig. 1D), and those with stability features of canonical nucleosomes being more scattered or more centrally located in the nuclei, resembling euchromatin (designated H2A.Z^{eu}; see Fig. 1E). (The third nuclear compartment containing the variant histone is H2A.Z^{lmm}; see above).

The localization patterns of the histone variant in the agarose-embedded nuclei labeled with ZAbA and ZAbB before fixation are similar to those of the prefixed specimen shown in the manufacturers' datasheets. The CFP or YFP-tagged H2A.Z.1 and Z2 containing nucleosomes appear to be scattered in the nucleus⁴², similarly to the images obtained with ZAbB and the GFP-tagged histone (Fig. 1E, Suppl. Fig. 4C).

In agreement with the ZAbA-detected nucleosomes exhibiting H3-like, i.e., decreased, salt-sensitivity in the salt elution experiments, H2A.Z was detected by mass spectrometry (MS) in the salt resistant fraction (see Suppl. Fig. 7A and Suppl. Table 2). Proteins associated with euchromatic functions as well as others implicated in heterochromatin organization^{43,44} were both detected, just like in a different experimental set-up, using the CUT&RUN protocol⁴⁵ followed by MS (flow-charts and titration of MNase concentration are shown in Suppl. Fig. 7B and C–E, respectively). According to the MS data, ZAbA and ZAbB recognize nucleosomes associated with an overlapping spectrum of proteins, many of which were found to be H2A.Z-associated

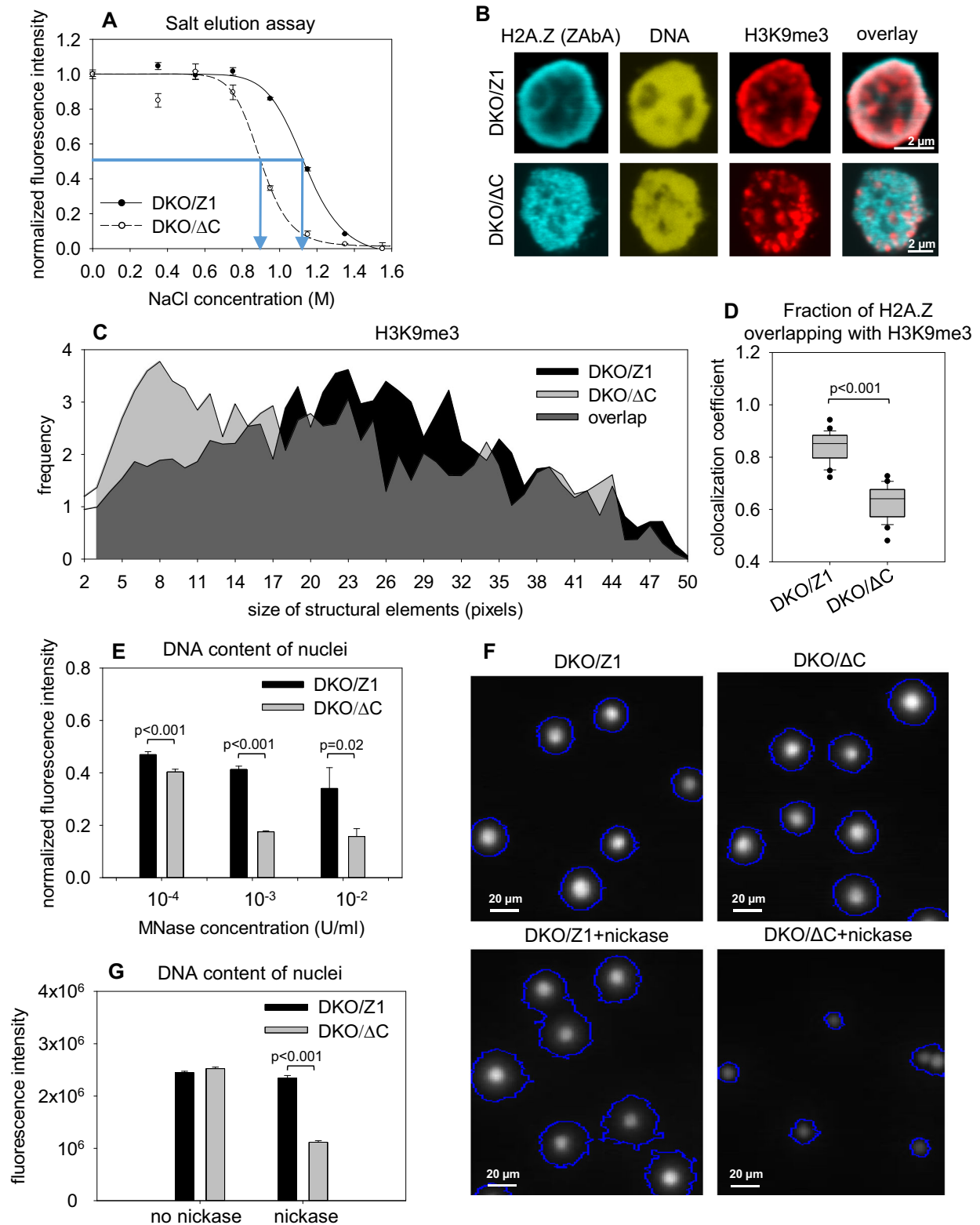
also in other studies. There was an overlap also between the list of hits in the two different approaches (H2A.Z, HPI, MATR3, LMNA, H1.0).

Effect of the H2A.Z C-terminus on nucleosome stability and localization

In view of the fact that the C-terminal region of the unstable H2A.Z.2.2 isoform is 14 residues shorter than either isoform of H2A.Z⁴, where the last six residues of Z.2.2 form a motif facilitating nucleosome assembly⁴⁶, we conducted experiments using cells expressing H2A.Z.1 with a 9 amino acid deletion at the end of their C-terminus (between amino acids I19–I28, Suppl. Fig. 1C), on a double, H2A.Z.1, H2A.Z.2 KO (DKO) DT40 background³⁷. The H2A.Z Δ C containing nucleosomes were less stable as compared to nucleosomes containing full-length H2A.Z, as studied by QINESIn in the agarose-embedded nuclei of the H2A.Z Δ C and the H2A.Z.1-expressor control cells, respectively; Fig. 2A, Suppl. Fig. 8A), while the stability of nucleosomes carrying H3K27me3 or H3K9me3 was similar in the two cells (Suppl. Fig. 8B, C). The elution profile of the C-terminally truncated H2A.Z-nucleosomes exhibiting canonical, H2A-like behavior was affected much less by nicking treatment, as compared to the nucleosomes containing full-length H2A.Z (using ZAbA; Suppl. Fig. 8D).

Remarkably, not only the stability of H2A.Z containing nucleosomes but also their nuclear localization pattern was C-terminus dependent (Fig. 2B–D). In the H2A.Z Δ C-expressing cells, the localization of ZAbA-detected H2A.Z is changed to a much more scattered and less peripheral topography in the same DKO background, while there was no such difference in the case of the ZAbB-detected ones (compare Suppl. Fig. 9 with Suppl. Fig. 10). The spatial distribution of H3K9me3 marked nucleosomes also changed, as reflected by the altered texture of H3K9me3 containing structural elements (Fig. 2C; Suppl. Fig. 11A, B) in comparison with that of H3K27me3 (Suppl. Fig. 11C, D), and the colocalization data of Fig. 2B, D, Suppl. Figs. 9 and 10. Manders colocalization coefficient (MCC) was used to characterize the pixel-overlap of H2A.Z with hetero- and euchromatin markers. The H2A.Z Δ C levels expressed in the nuclei of these DKO DT40 cells were about half of the H2A.Z levels in the same DKO background, while the total number of H3K9me3, H2B nucleosomes and also the amount of DNA in the nuclei of the two cell types were similar (Suppl. Fig. 11E). The degree of colocalization between ZAbA-detected H2A.Z and H3K9me3 was significantly lower in the H2A.Z Δ C than in H2A.Z.1 DKO nuclei (Fig. 2D). The difference between the two cell lines was smaller in the case of H2A.Z and H3K27me3 colocalization (Suppl. Figs. 9 and 10). The somewhat elevated levels of H3K27me3 in H2A.Z Δ C cells (Suppl. Fig. 11E) may account for the altered degree of colocalization between H3K9me3 and H3K27me3 (Suppl. Fig. 10D). The conspicuous decrease of colocalization between H2A.Z and H3K9me3 in H2A.Z Δ C is present in spite of the fact that the ZAbA-detected H2A.Z Δ C levels are lower than those of H2A.Z detected in DKO/Z1 cells (Suppl. Fig. 11E). The higher MCC value indicative of more H2B colocalizing with ZAbA-detected H2A.Z in the Δ C nuclei relative to those harboring the full-length form (Suppl. Fig. 9C) can be explained by the decrease in peripherally localized H2A.Z levels, but not of H2B. At the same time, there was no change in the colocalization coefficients in the case of PWWP2A and H2B (Suppl. Fig. 9D).

In contrast with the above observations, when the histone variant was labeled using ZAbB, preferentially recognizing euchromatic H2A.Z as shown above, no significant differences were measured between the two kinds of cells in terms of colocalization of the histone variant with either the euchromatic mark H3K4me3 or the heterochromatic mark H3K27me3 (Suppl. Fig. 10A, B). Although the ZAbB-detected H2A.Z was similarly scattered in both wild-type (wt) and Δ C nuclei, the fraction of ZAbB-detected H2A.Z colocalizing with H3K9me3 decreased significantly in the Δ C nuclei (Suppl. Fig. 10C), similarly to the decrease of colocalization between ZAbA-detected H2A.Z and H3K9me3 (Fig. 2D).



Furthermore, the degree of colocalization between the two heterochromatic marks H3K27me3 and H3K9me3 was significantly different in the H2A.Z.1 vs ΔC nuclei (Suppl. Fig. 10D), suggesting that the global nuclear organization has changed in the ΔC nuclei. The topographic characteristics of ZAbA- and ZAbB-detected H2A.Z in the DKO/Z1 and H2A.ZΔC nuclei described above were also apparent in super-resolution microscopic images, as shown in Suppl. Fig. 11F, G. There was a difference between the DKO/Z1 and ΔC DT40 nuclei also in the

distribution of H3K9me3 remaining lamina-attached in the halo samples, while no such difference was detected in the case of H3K27me3 (Suppl. Fig. 12).

Consequences of H2A.Z C-terminal truncation on accessibility of DNA in chromatin and on gene expression

The chromatin architectural changes related to the C-terminal truncation of H2A.Z were reflected also in other global effects of potential

Fig. 2 | Effect of C-terminal truncation on the salt sensitivity, nuclear localization and chromatin accessibility features. **A** Salt elution profiles of nucleosomes in H2A.Z.1ΔC (DKO/ΔC) and H2A.Z.1 expressor DKO DT40 cells (DKO/Z1), detected by ZAbA. The elution curves refer to G1 phase nuclei gated according to their DNA fluorescence intensity distribution and the error bars represent SEM of ~600 nuclei measured by LSC. **B** Representative CLSM images showing the nuclear localization of H2A.Z recognized by ZAbA, and H3K9me3 co-labeled with H2A.Z in DKO H2A.Z.1ΔC (DKO/ΔC) and H2A.Z.1 (DKO/Z1) nuclei. **C** Texture analysis (see “Methods”) of ΔC (DKO/ΔC) and CTRL (DKO/Z1) nuclei showing the size distribution of structural elements containing H3K9me3 (see also Suppl. Fig. 11A–D). **D** Colocalization analysis of H2A.Z and H3K9me3 in ΔC (DKO/ΔC) and CTRL (DKO/Z1) nuclei. The Manders colocalization coefficient (MCC) values reflecting the

fraction of H2A.Z overlapping with H3K9me3 are shown. Box-and-whisker plot was created from the data of 25 nuclei. For the expression levels of the proteins in the two cell lines, see Suppl. Fig. 11E. **E** MNase sensitivity of ΔC (DKO/ΔC) and CTRL (DKO/Z1) nuclei. Total DNA content per nuclei was measured by LSC before and after endonuclease treatment, as indicated on the figure. (**F, G**) Comparison of chromatin sensitivities to a frequent cutter nickase (Nt.CviPII). DNA content (**G**) and halo size (Suppl. Fig. 13B) of ΔC and CTRL nuclear halos were measured by LSC before and after nickase treatment of the nuclei (see “Methods”), as indicated on the figure. Error bars represent SEM of ~600 nuclei. Box-and-whisker plot shows the median, 25th and 75th percentiles as vertical boxes with error bars, 5th, 95th percentiles and outliers as dots (also in the other figures).

functional relevance. As compared to DKO H2A.Z.1 nuclei, those of the DKO H2A.Z.ΔC cells were more readily digested using a frequent cutter nickase, MNase and DNase I (Fig. 2E–G; Suppl. Fig. 13A, B). These H2A.Z tail-dependent changes in chromatin accessibility features were also reflected in differences of gene expression patterns, comparing wt, DKO H2A.Z.1, and DKO H2A.Z.ΔC cells (Suppl. Fig. 14). Among the genes substantially up- or down-regulated in DKO H2A.Z.ΔC relative to DKO H2A.Z.1 or wt, those that have been implicated with pathways where H2A.Z is known to participate in, are listed in Suppl. Table 3. These pathways include processes directly involving H2A.Z such as DNA repair⁴⁷. Indeed, DKO H2A.Z.ΔC cells appear to exhibit a diminished DNA damage response and relatively poor survival upon exposure to DNA damaging agents (Suppl. Fig. 15).

Effects of C9 treatment in permeabilized HeLa nuclei

As Fig. 3, Suppl. Figs. 16, 17 and 18 demonstrate, the destabilized character, increased nuclease sensitivity and altered intranuclear distribution of nucleosomes containing H2A.Z.ΔC were emulated when a peptide representing the last 9 amino acids of the C-terminus (C9) was added to HeLa nuclei, suggesting that these differences are the direct consequences of molecular interactions involving the tail region; shorter peptides (C6–C8) or a scrambled control peptide (SCR; see “Methods”) were not, or much less effective. Upon treatment with C9, the H2A.Z-containing nucleosomes fell apart at 1M salt to a higher extent (Fig. 3A), while addition of the peptide to nuclei at low salt elicited no eviction (Suppl. Fig. 17A, B). The H2A.Z-containing chromatin regions became partially separated from the H3K9me3-rich periphery based on the significantly MCC (Fig. 3B, C; Suppl. Fig. 17C, D). This separation was also observed with Flag-tagged H2A.Z as shown in Suppl. Fig. 18 (i.e., using the tag with the least influence on the stability of H2A.Z according to Suppl. Fig. 4F). Notably, treatment of the nuclei with the C9 peptide increased sensitivity to nickase and MNase used at 10^{-3} U/ml concentration (Fig. 3D–L). This MNase concentration is in the lower end of the usual concentration range of the enzyme applied in MNase-seq studies when performed on fixed⁴⁸ or nonfixed cells⁴⁹; however, the enzyme was applied in the absence of loosely bound proteins that were released upon preparation of the nuclei in our studies.

In order to determine if the C9-induced increment in MNase sensitivity is restricted to or preferentially comprises particular regions, three approaches were followed. First, the sensitivity of chromatin to MNase was measured in the H3K4me3-marked (mostly euchromatic) and H3K9me3-marked (mostly heterochromatic) domains (Fig. 3G, H) over the HeLa nuclei by LSC. The DNA content of the mostly heterochromatic peripheral and the more euchromatic central nuclear regions were also separately assessed by CLSM. As shown in Fig. 3I–L, C9 treatment increased MNase digestibility in both chromatin domains. In a second approach, CUT&RUN⁴⁵ experiments were performed. To mirror the conditions of the LSC-based MNase experiments, the peptide-treated and control nuclei were first incubated with MNase, then with the antibodies, followed by the targeted digestion using the pAG-MNase fusion protein (see “Methods”). The

localization of the peaks was nearly identical to that of the peaks reproducibly detected in the routine procedure (without prior MNase digestion), both representing only a fraction of the CHIP-Seq peaks detected using the same antibody (Suppl. Fig. 19A). This difference highlights the role of accessibility in CUT&RUN, performed on close-to native chromatin, as opposed to CHIP-Seq experiments where fixed and sonicated samples are immunoprecipitated.

Using 10^{-3} U/ml MNase in the first step, the sequences of the mononucleosomal products of the subsequent pAG-MNase digestion represent the sequence environment of the nucleosomes detected by IF in LSC at about 50% digestion of all DNA, both in euchromatin and heterochromatin (see Fig. 3G, H). As Fig. 4 shows, the number of H3K4me3 peaks detected in the C9 sample was about 1.3x and 1.4x higher than in the CTRL and SCR samples, respectively, while the number of H3K9me3 peaks increased ~2x and ~2.2x relative to the numbers of the CTRL and SCR samples, respectively. (For example, the total number of peaks were 36,561 and 17,458 for the C9 and CTRL sample, respectively, in the experiment of Fig. 4B). These ratios were similar in an independent experiment (see Suppl. Fig. 19B). Thus, the result of the initial increment in MNase cleavages evoked by C9 pre-treatment (resulting in increased loss of DNA from the embedded nuclei; see Fig. 3G, H) is the appearance in the CUT&RUN digests of additional DNA fragments of H3K4me3- and H3K9me3-nucleosomal origin, according to the scheme of Suppl. Fig. 19D. The H3K4me3-nucleosomes in the CUT&RUN samples were mostly promoter-proximal also in the C9-treated sample, with a subpopulation of new peaks arising from regions outside the promoters (Fig. 4A). The H3K9me3 peaks detected only in the C9-treated sample were distributed among the different chromatin domains similarly to the peaks of the control (Fig. 4B and Suppl. Fig. 19C), demonstrating that the peptide did not increase digestibility of the different H3K9me3-marked heterochromatic regions significantly differently. The peaks detected only in the C9 samples must have come from sites randomly distributed among the different categories of nucleosomes marked with particular PTMs, similarly to two independent replicas of the same sample with different total peak numbers.

The result of C9 treatment of HeLa nuclei in euchromatic regions was studied also by ZAbA-targeted CUT&RUN combined with mass spectrometry (see “Methods”). As Fig. 4C and Suppl. Table 4 demonstrate, an increased presence of several nuclear proteins associated with euchromatic functions, including H2A.Z, was observed, in line with decondensation and increased accessibility to ZAbA and/or to MNase in the chromatin around H2A.Z-containing nucleosomes in the euchromatin. The H2A.Z-nucleosomes of peripheral heterochromatin remained in the nucleus in these experimental conditions (Suppl. Fig. 20). In a third approach, the residual genomic DNA remaining in the agarose embedded samples was sequenced and the distributions of read coverages among different sequence categories representing euchromatin and heterochromatin were compared in the individual samples of C9-treated and control nuclei after MNase digestion. The distribution of reads is expected to reflect the amount of DNA in the different sequence categories and

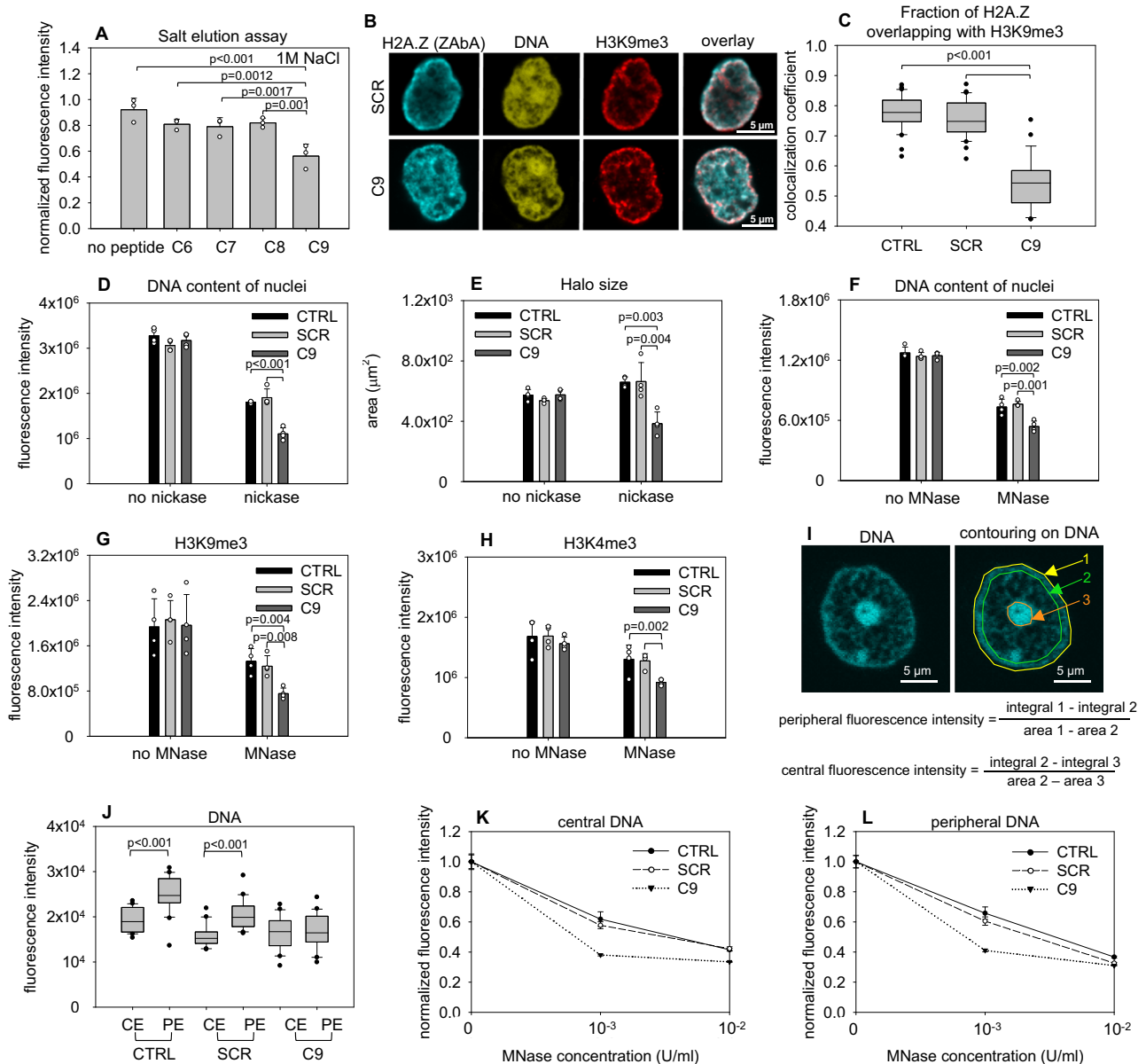


Fig. 3 | The effect of peptides representing the C-terminus of H2A.Z.1 on the stability, nuclear localization, and nuclease digestibility of different nucleosomes. A Stability of H2A.Z nucleosomes, measured as the residual ZAbA IF in permeabilized HeLa nuclei exposed to 1M NaCl in the presence of different length peptides (C6–C9) compared to the control (no peptide). -600 G1 nuclei were measured in each sample by LSC. Means \pm SD of 3 biological replicates are shown. **B** Representative CLSM images showing the localization of H2A.Z recognized by ZAbA and of H3K9me3 co-labeled with H2A.Z, in HeLa nuclei treated with C9 or the scrambled control peptide (SCR). **C** Colocalization analysis of H2A.Z and H3K9me3 on CLSM images from the experiment of (B). The MCC values representing the fraction of H2A.Z overlapping H3K9me3 are shown. Box-and-whisker plot was created from data of -30 nuclei. **D, E** Global nickase sensitivity of HeLa nuclei after treatment with C9 or SCR, measuring DNA content based on SYBR Gold staining (D)

or halo size (E), by LSC. Means \pm SD of 4 biological replicates are shown; events were collected from the whole cell population. **F–H** Global MNase sensitivity of HeLa nuclei after treatment with SCR or C9, measuring DNA content (F; SYBR Gold-staining), H3K9me3 (G) and H3K4me3 IF (H) by LSC. Means \pm SD of 4 biological replicates are shown; events were collected from the whole cell population. **I** Contouring and calculation of mean pixel intensities at the nuclear periphery or in the center of HeLa nuclei used in the experiments of (J–L). **J** Mean pixel intensities of PI-stained DNA measured at the periphery (PE) or in the center (CE) of HeLa nuclei after SCR or C9 treatment and without peptide addition (CTRL). Box-and-whisker plot was created from the data of 20 nuclei. **K, L** CLSM measurement of MNase sensitivity of SCR-, C9-pretreated and control HeLa nuclei, measuring PI-stained DNA in the center or at the periphery. The mean pixel intensities normalized to 0 U/ml MNase are shown; error bars represent the SEM of 20 nuclei.

their relative resistance to sonication⁵⁰, yielding an unbiased global picture of the relative C9-elicited sensitization of the different sequence categories to MNase. The peptide, while significantly increasing access of the enzyme to both H3K4me3 and H3K9me3 nucleosomes (according to the LSC data of Fig. 3G, H and the results

of the CUT&RUN experiments described above), and enhancing the overall digestion of the genomic DNA (Fig. 3D, F, K, L), did not influence the proportions (in neither of the experiments shown in Suppl. Fig. 2I), confirming that MNase sensitivity was increased by the peptide rather uniformly genome-wide.

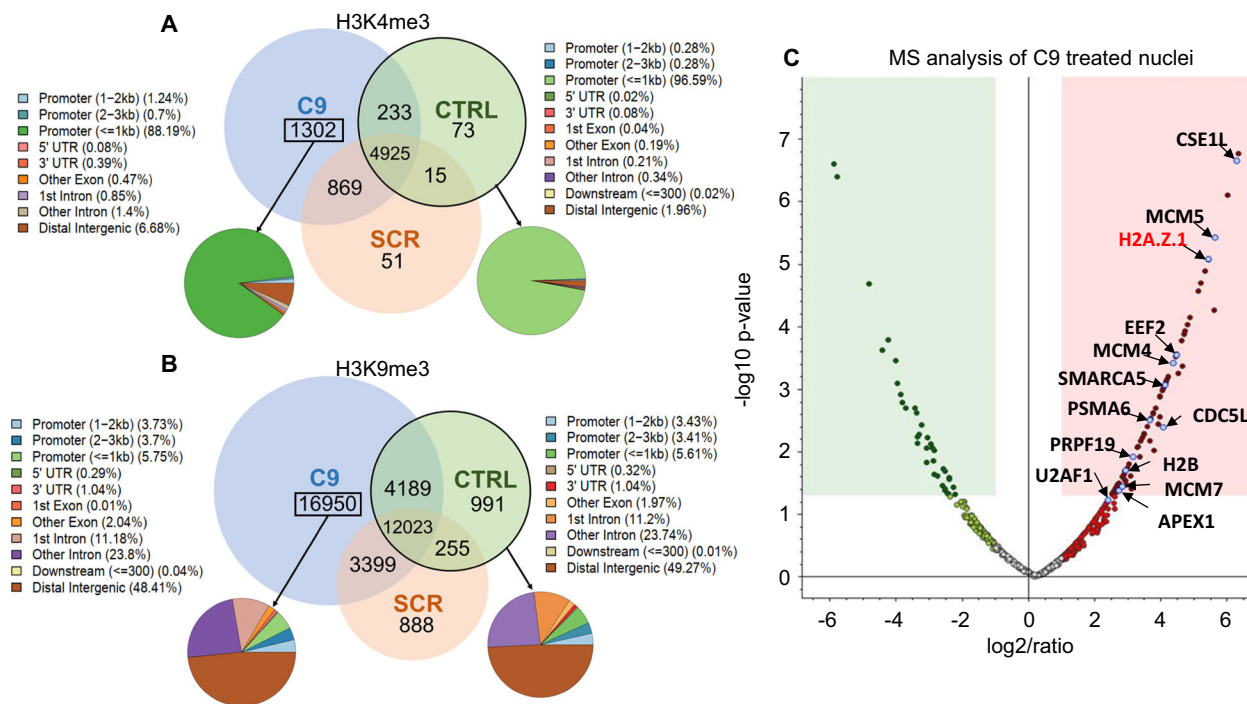


Fig. 4 | Effect of C9 on euchromatic or heterochromatic regions in permeabilized nuclei analyzed by CUT&RUN combined with mass spectrometry.

A, B Venn-diagrams showing the number of H3K4me3 (**A**) and H3K9me3 (**B**) peaks detected in CUT&RUN experiments of C9-, SCR-treated and untreated (CTRL) samples of HeLa nuclei (see text as well as “Methods” for details). The pie charts show the distribution of the annotated C9-only peaks among major sequence categories, or the distribution of all the peaks in the untreated (CTRL) samples.

Dark (C9) and light (CTRL) green areas: peaks localized at TSS+/- 1 kb. Brown and purple colors: peaks at distal intergenic regions and introns (For replica of Fig. 4B, see Suppl. Fig. 19B). **C** Volcano plot illustrating protein fold changes in the C9-treated sample compared to the untreated control identified by mass spectrometry in a ZAbA- pAG-MNase -CUT&RUN experiment using HeLa nuclei (see “Methods”). Proteins listed in Suppl. Table 4 are indicated.

Interaction of reconstituted nucleosomes with C9 as studied by fluorescence correlation spectroscopy (FCS)

FCS measurements were conducted to further investigate to what extent the carboxyfluorescein-labeled C9 (C9-CF) is able to bind reconstituted H2A or H2A.Z-containing nucleosomes and/or the Cy5-labeled nucleosome-positioning Widom sequence used for reconstruction.

The autocorrelation function (ACF) of the samples with nucleosomes was shifted to longer lag times suggesting slower diffusion due to binding (Fig. 5A, B). The fits of the ACFs allowed us to identify a fast-diffusing population in all samples corresponding to non-bound peptides and a slower diffusing population in the nucleosome containing samples attributed to peptides bound to nucleosomes. A slow component was also observed in samples containing naked DNA. The relative proportion of the slow, bound component was also obtained from the fits (Fig. 5C; Suppl. Fig. 22). The ACF curves of C9-CF alone could be fitted reasonably well with a single diffusing component (see Fig. 5B); therefore, no C9-C9 binding is assumed to occur in our conditions.

In fitting the autocorrelations curves, the diffusion time of the slow fraction was determined based on the diffusion of the Cy5-labeled DNA, after correction for the difference in focal volumes at the different wavelengths (following the pipeline shown in Suppl. Fig. 23). These measurements were conducted at equilibrium conditions established at a 5-fold molar excess of nucleosomes or DNA over C9-CF (or the labeled scrambled peptide, SCR, used as a control).

As Fig. 5C demonstrates, at low salt condition about ~5% of the peptide was found in the slower fraction representing C9-CF bound to any of the macromolecules, in several independent experiments. The CF-SCR did not bind to nucleosomes or DNA, while binding of C9-CF to nucleosomes built up from either canonical H2A or H2A.Z was well detectable (Suppl. Fig. 22).

From the 5% value, a K_d of $\sim 2 \mu\text{M}$ was calculated based on the law of mass action (as in ref. 51). When the FCS measurements were conducted in solutions containing 700 mM NaCl, expected to loosen the binding of the canonical histone dimers⁵², binding of the peptide to the nucleosomes was considerably increased, yielding ~35% of the peptide in the slower fraction, which translates into a $K_d = 90 \text{ nM}$. Binding of the peptide to DNA was not increased significantly at this salt concentration. These data raise the possibility that the C-terminal tail may be involved in establishing intra- or internucleosomal associations.

Effects of C9 introduced into live cells

Under conditions that did not significantly affect cell viability (Suppl. Fig. 24), C9-CF could be efficiently introduced into live HeLa cells using the cyclodextrin derivative SBECD as shown in Fig. 6A and Suppl. Fig. 25. The dotted CLSM pattern of C9 accumulation when added to live cells (observed using C9-CF; Fig. 6A) is probably the consequence of the uptake process. The nuclear features that appear to depend on the C-terminus of H2A.Z were modulated by C9 also when introduced into live cells. As Fig. 6B, C and Suppl. Fig. 25A-F demonstrate, reorganization of peripheral H2A.Z-containing heterochromatin relative to H2B-GFP or H3K9me3, decreased nucleosome stability (Fig. 6D; Suppl. Fig. 25G) and increased nuclease (nickase) sensitivity (Fig. 6E, Suppl. Fig. 25H) could be detected in the nuclei of C9-treated HeLa cells one day after a single dose of peptide treatment. Similar though less conspicuous changes were demonstrated in the nuclei of two melanoma cell lines (refs. 31,53; see Fig. 7A, B), with the reorganization of H2A.Z-chromatin demonstrated via its altered colocalization with H3K9me3. When the effect of C9 treatment was studied in MEL1617 cells by RNA-seq, 564 genes were significantly down-regulated and 58 up-regulated (Fig. 7C). Intriguingly, almost none of the down-regulated genes localize to the Giemsa-dark bands in the chromosome ideograms. At

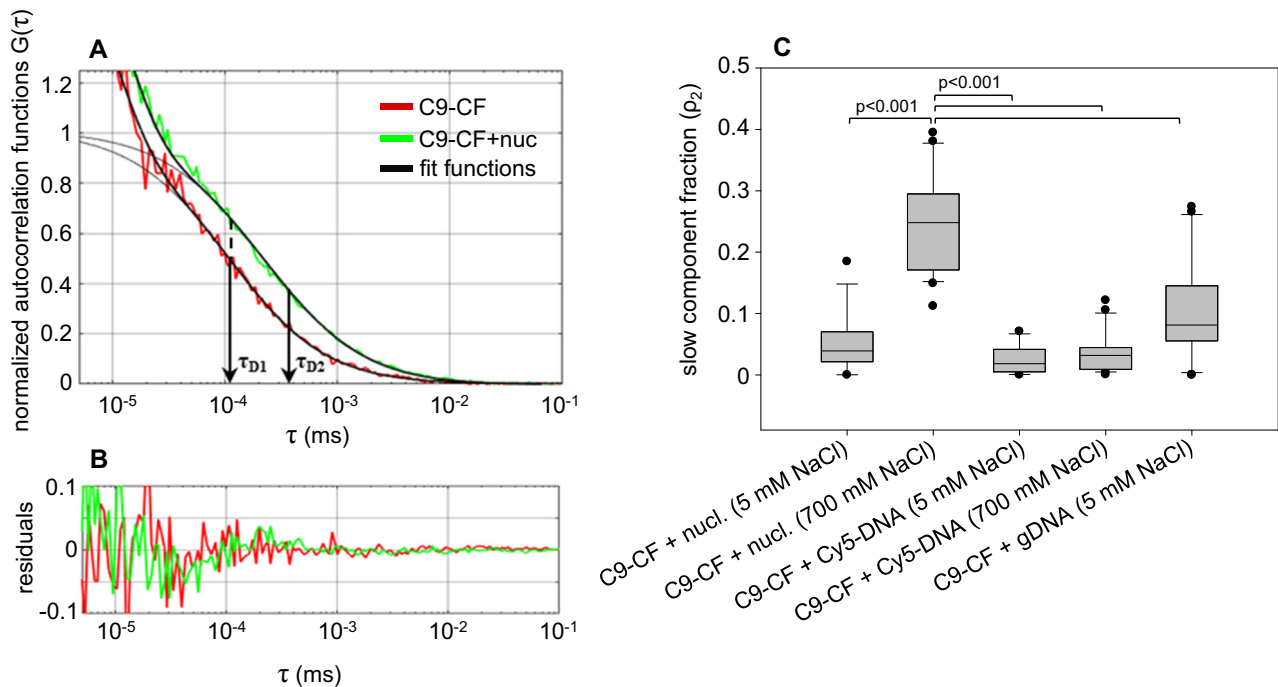


Fig. 5 | FCS analysis of C9-CF binding to reconstituted mononucleosomes. **A** Representative normalized autocorrelation functions (ACF-s) of C9-CF are shown; the correlation curves were acquired in the absence (red) or presence (green) of nucleosomes, at 700 mM NaCl concentration. Fits assuming triplet transition and a single diffusing species for a sample without nucleosomes and two diffusing populations with nucleosomes were used (black solid lines). The gray line indicates the fit excluding triplet state transition. τ_{D1} and τ_{D2} are the diffusion times of the fast and slow components, characterizing the diffusion of freely diffusing

and nucleosome-bound C9-CF peptides, respectively. The ACF-s shifted toward slower diffusion times indicating the presence of a nucleosome-bound fraction. **B** Fit residuals. **C** Slow fraction of C9-CF. The peptide was incubated with nucleosomes at 5 mM or 700 mM NaCl concentration, with Cy5-labeled Widom-sequence at 5 mM or 700 mM NaCl, or with genomic DNA at 5 mM NaCl. The slow fraction ρ_2 was calculated in ACF fits as described in the “Methods” and presented as a box-and-whisker plot.

the same time, genes of different expression levels in the C9-untreated control cells and the H2A.Z ChIP-seq peaks of (SK-MEL-147) melanoma cells are rather evenly distributed among the Giemsa-light and dark bands (Fig. 7E–K). The genes being randomly down- and upregulated upon culturing are distributed among the Giemsa bands also quite evenly (Fig. 7K). Gene subsets of particular pathways are over-represented among the significantly down-regulated genes (Fig. 7L). C9 treatment elicited changes also in the expression of repetitive elements (see Supplementary Methods and Supplementary Discussion).

Discussion

The data presented demonstrate the decisive role of the C-terminal unstructured tail of H2A.Z both in determining stability features of nucleosomes containing this variant and in their intranuclear landscape. Further, this study reveals the H2A.Z tail-dependence of certain local and global chromatin accessibility characteristics and offers means to modulate chromatin structure and function based on interactions involving its tail.

H2A.Z tail-dependent and C9-elicited changes involve euchromatin as well as heterochromatin

The elution curves of QINESIn reflect the off-rate of particular histones released from the nucleosomes in situ, i.e., we look at nucleosome stability through the spectacles of H2A.Z dissociation, native or tagged, induced by salt treatment. Based on the localization patterns (see e.g., Fig. 1D, E), the tail-dependent changes and differences thereof (e.g., as shown in Figs. 2B–D, 3B, C, 6B, C and 7A, B; Suppl. Figs. 9, 10A–D, 11 and 25A–F), colocalization with HPI (Suppl. Fig. 10F), and the different stability features (Figs. 1A–C, 2A, 3A and 6D; Suppl. Fig. 17A), we propose that ZAbA preferentially detects stable

nucleosomes residing in peripheral heterochromatin (H2A.Z^{hc}), while ZAbB recognizes the histone variant preferentially in unstable nucleosomes within the euchromatin (H2A.Z^{eu}). Shielding of particular H2A.Z epitopes by the different molecular partners specific to the compartments could account for the different reactivity of the two classes of antibodies. The stable H2A.Z containing nucleosomes become destabilized to a canonical H2A-like state when the C-terminal tail is deleted or its binding to molecular partners may be disabled by the addition of a competing peptide. The tags apparently also hamper some of these interactions, with a destabilizing effect (Suppl. Fig. 4F). The N-terminal part of H2A.Z has a marked effect on the sliding of the nucleosome on the DNA³⁵, while the C-terminal tag is expected to directly interfere with interactions involving the tail. Tagged H2A.Z also appears to be localized in a scattered rather than dominantly peripheral manner in the nucleus, compared with ZAbA-detected native H2A.Z (Suppl. Fig. 4C, E), with the Flag-tagged version reminding of native H2A.Z best (Suppl. Figs. 4C, E and 18).

The remarkable tail-dependence of chromatin organization as detected by ZAbA or anti-H3K9me3 staining in the DT40 system (Fig. 2) and the C9-elicited changes in HeLa nuclei (Fig. 3) suggest that these changes most certainly involve the heterochromatin. This is further supported by the fact that MNase digestibility was increased also at the periphery of the nuclei, comprising constitutive heterochromatin (Fig. 3L). The finding that C9 pretreatment augments the MNase digestion of H3K9me3-marked domains (Fig. 3G) is in quantitative accordance with the ~2–2.3x increment revealed in the CUT&RUN studies. Since different sequence categories within these domains are rather uniformly affected by C9 (Fig. 4), heterochromatin in general appears to be sensitive to destabilization by treatment with excess C9. On the other hand, the gene expression differences between wt or DKO H2A.Z.1, and H2A.ZΔC-expressor DKO DT40 cells

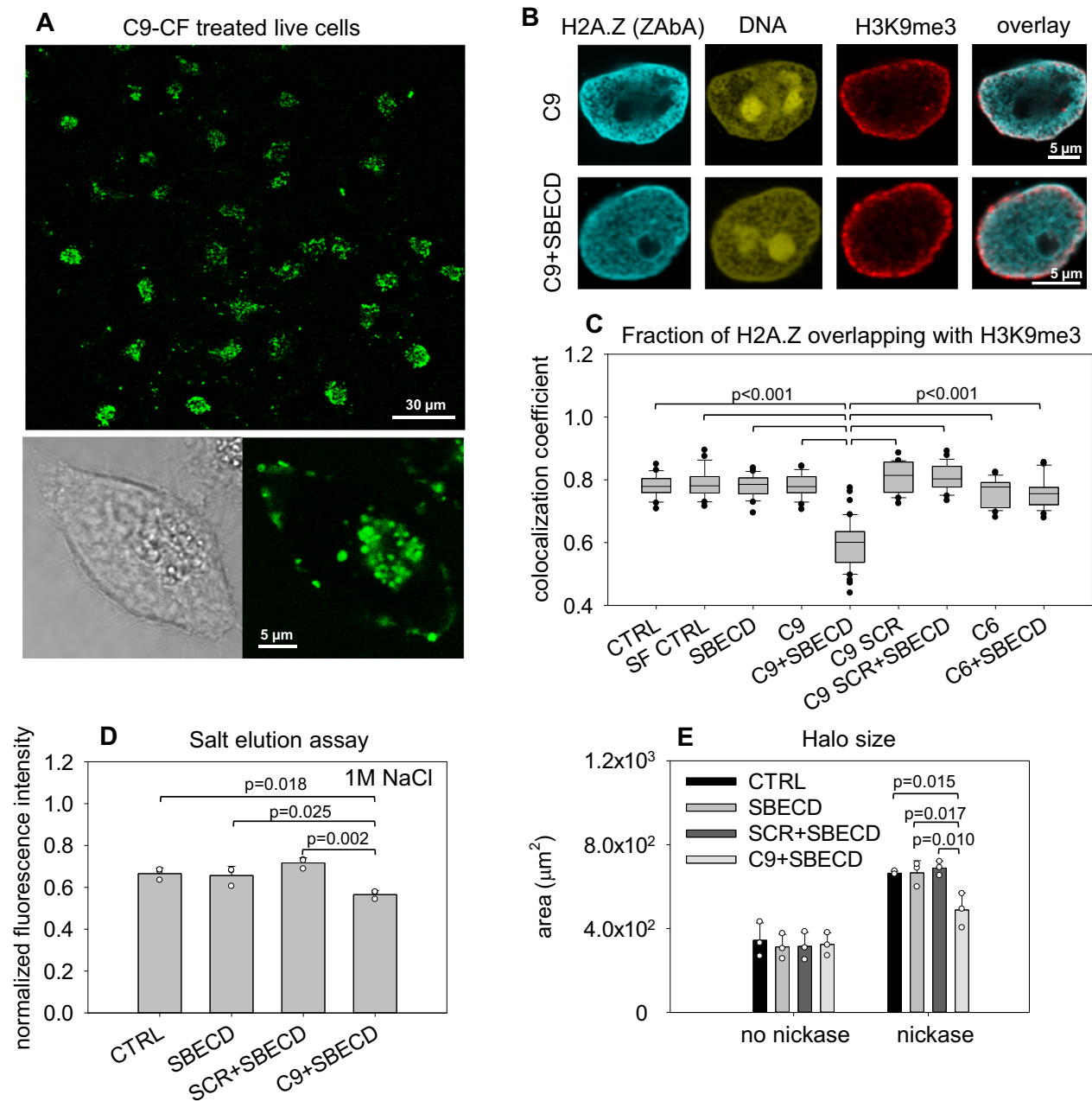


Fig. 6 | Localization and effects of C9 peptide introduced into live HeLa cells by the cyclodextrin derivative SBECD. **A** Localization of C9-CF (carboxyfluorescein conjugated C9) in live HeLa cells after 2 h treatment with C9-CF/SBECD followed by overnight culturing, as visualized by CLSM. Zoom-in image of a cell from the C9-CF/SBECD treated sample is shown at the bottom. **B** Representative confocal images of H2A.Z-H3K9me3 co-labeled nuclei following introduction of C9 into live HeLa cells. Cells were treated with the C9, C9 SCR or the C6 peptide using SBECD (C9 + SBECD, C9 SCR + SBECD or C6 + SBECD), or with serum-free medium in the absence of peptides and cyclodextrins (SF CTRL). **C** MCC values representing the fraction of

H2A.Z overlapping with H3K9me3 calculated for the nuclei shown in **(B)**. Box-and-whisker plots were created from the data of ~30 nuclei. **D** Resistance of H2A.Z nucleosomes to 1 M NaCl in permeabilized HeLa nuclei prepared from untreated, cyclodextrin-treated, SCR + SBECD- or C9 + SBECD-treated HeLa cells. Bar charts show the mean fluorescence intensity, error bars represent the SD of 3 biological replicates. **E** Measurement of chromatin sensitivity to nickase. Halo size of untreated (CTRL), SBECD-, SCR + SBECD- and C9 + SBECD-treated nuclei were measured by LSC before and after nickase treatment. Bar charts show the mean fluorescence intensities, error bars represent the SD of 3 biological replicates.

(Suppl. Fig. 14, Suppl. Table 3), the effect of C9 treatment on MNase sensitivity at around H3K4me3-marked regions (Figs. 3H and 4A), on the release of proteins associated with transcription, replication and repair (Fig. 4C; Suppl. Table 4) in the case of nuclei, and of the changed expression of altogether ~620 genes in the case of live cell treatment (Fig. 7) collectively imply H2A.Z tail-dependent changes to be present also in euchromatin.

ChIP sequencing (ChIP-seq) data available for different cell types reveal that two of the antibodies detecting unusually stable

nucleosomes (Abcam 4174 and Millipore 07-594; see Suppl. Fig. 2A and C, respectively, and refs. 54,55) give peaks both in euchromatin and heterochromatin. The ChIP-seq data obtained using H2A.Z-GFP and anti-GFP antibodies were very similar to parallel ChIP-seq data obtained with Abcam 4174⁵³. However, the experimental conditions of ChIP-seq and IF studies are very different, as antibody labeling occurs after sonication in the first, while it is applied in the close-to-native state of the agarose-embedded, permeabilized nuclei in the second. Indeed, the CUT&RUN maps comprise a subpopulation of the ChIP-seq

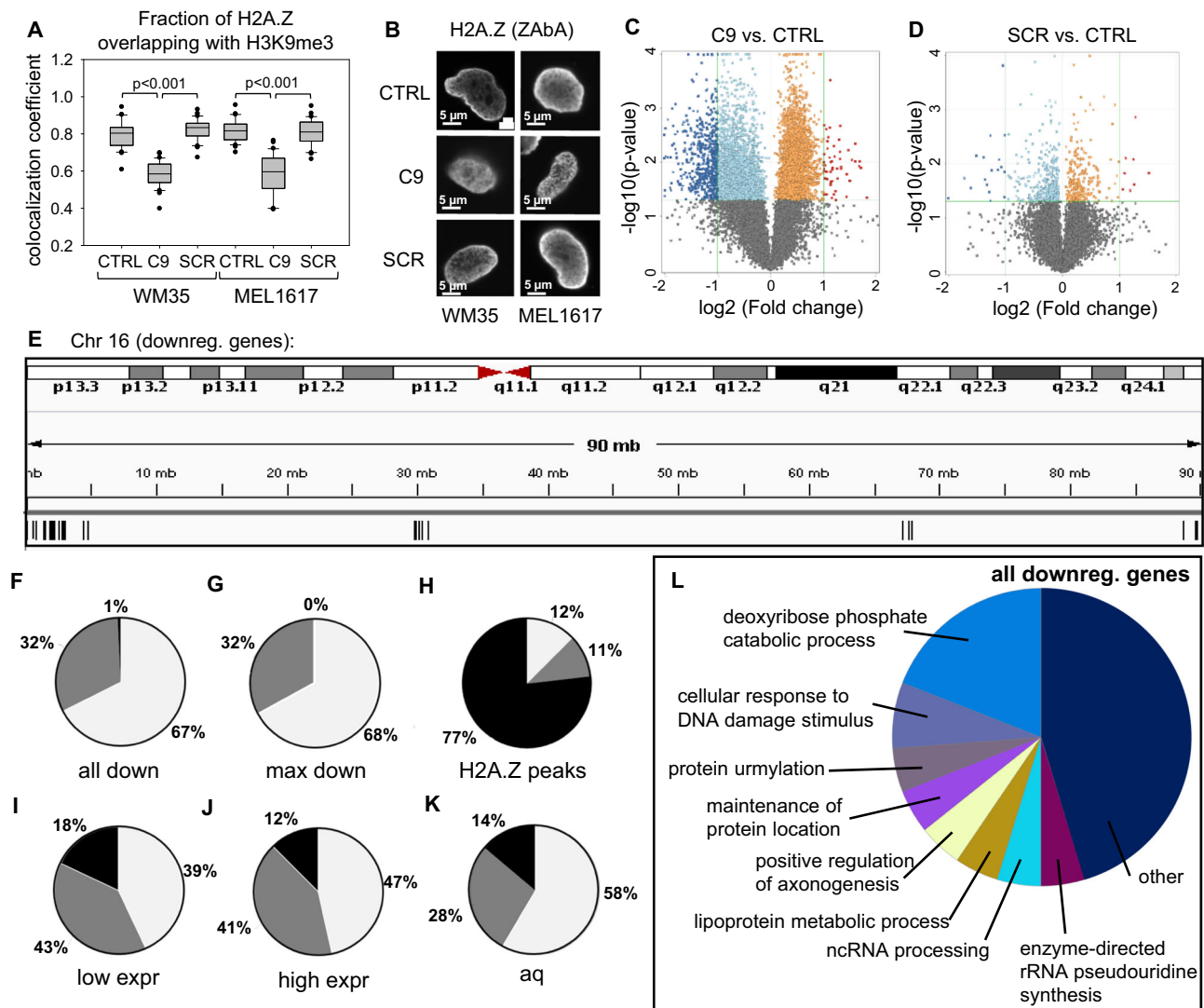


Fig. 7 | Effect of C9 treatment of live melanoma cell lines. A Colocalization of H2A.Z and H3K9me3 in WM35 and MEL1617 cells treated with C9, SCR or left untreated (CTRL). MCC values representing the fraction of H2A.Z overlapping with H3K9me3 are shown. Box-and-whisker plots were created from the data of 30 nuclei. **B** CLSM images from the samples of (A) showing H2A.Z rearrangement. **C, D** Volcano plots showing differentially expressed genes defined as $\log_2(\text{Fold change}) < -1$ or $> +1.0$ and $p < 0.05$ (dark blue and red dots). C9 vs. CTRL (C) and SCR vs. CTRL (D) data of MEL1617 cells are shown (See the volcano plot of the differentially expressed genes in SCR vs. C9 in Supplementary Fig. 26.). **E** IGV screenshot of the chromosome 16 ideogram. The genes down-regulated by C9 treatment are shown below. **F** Pie chart showing the distribution of all down-regulated genes among different Giemsa bands. **G** Pie chart showing the distribution of highly

down-regulated genes (fold change < -2.35 ; $-1/3$ of all down-regulated genes) among different Giemsa bands. **H** Pie chart showing the distribution of HeLa H2A.Z ChIP-seq peaks (downloaded from ENCODE database, accession ENCF094MFL) among different Giemsa bands. **I, J** Pie charts showing the distribution of all expressed genes grouped by the expression level of the corresponding gene. Distribution of genes with low (< -0.2) and high (> 0.5) expression in control MEL1617 cells are shown in (I) and (J), respectively. The distributions represented by the pie charts are normalized to the fraction of the corresponding areas in the genome. **K** Band localization of the genes significantly down- or upregulated spontaneously upon culturing of control MEL1617 cells. RNA-seq data from different thawed up aliquots (aq): see SRA BioProject PRJN853352. **L** Functional characterization of the genes down-regulated by C9 (C9 vs SCR).

peak-set obtained with the same antibody (Suppl. Fig. 19), in line with ref. 56 Binding of C9-CF to reconstituted nucleosomes (see FCS data of Fig. 5 and Suppl. Fig. 22) is in line with its genome-wide effects on nucleosome stability demonstrated in the experiments of Figs. 2–4.

The presence of H2A.Z in the nuclear lamina

The fraction of the histone variant remaining in the nuclei after the maximal salt concentration used in the elution experiments (Suppl. Fig. 2F) was further investigated by mass spectrometric analyses and immunostaining of these nuclear halo preparations (see “Methods”). As Fig. 1F and Suppl. Table 1 show, a fraction of H2A.Z (H2A.Z^{lmm}), as well as proteins implicated in lamina tethering and/or chromatin loop organization, could be detected. All these proteins appear to be in

tight association with the nuclear lamina. We speculate that H2A.Z^{lmm} can interact with the nucleosomes and/or the internucleosomal DNA of peripheral heterochromatin, contributing to the lamina tethering of chromatin loops. The decreased presence of lamina-associated H3K9me3 signal in the ΔC DT40 cells (Suppl. Fig. 12) is in line with this hypothesis.

We note that the prominent H3K9me3 and H3K27me3-rich spots at the periphery of the nuclear halos give the impression of loop anchorage points detached from the lamina upon salt exposure (Suppl. Fig. 12). H3K9me3 detected at the periphery of the halos were more prominent in the case of the full-length H2A.Z containing nuclei as compared with those of the ΔC -expressors, suggesting involvement of tail-mediated molecular interactions in higher-order chromatin

organization. Such a role of the H2A.Z nucleosomes could perhaps account for the tail-dependence of global nuclease sensitivity detected in the DT40 system (Fig. 2).

The separation of the two layers of the nuclear lamina with different Lamin B1 content (Fig. 1F) confirms the conclusions of the superresolution studies first describing this structural feature⁴⁰. This simple way of visualization, also in view of the laminar presence of proteins involved in higher-order chromatin organization (Suppl. Table 1), opens possibilities for further experimental investigation of the role of nuclear lamina in chromatin loop tethering.

Tail-dependent switching of H2A.Z nucleosomes between the stable vs. unstable state, and between peripheral vs. scattered topography

The H2A.Z-containing nucleosomes detected by ZAbA are unusually stable in the sense that H2A.Z is evicted from the nucleosomes at higher salt concentrations than typical for H2A, when studied by QINESIn *in situ*. This was reproduced employing *in vitro* assembled chromatin (Fig. 1G), in line with previous studies where chicken erythrocyte chromatin was subjected to hydroxyapatite chromatography³⁹, suggesting that this is an intrinsic feature of the reconstituted nucleosome array containing this variant, i.e., it can be observed in the absence of nucleosome-unrelated potential interacting partners.

Nuclear architecture, when portrayed by ZAbA- or ZAbB-detected H2A.Z and H3K9me3, could be modulated via addition of the C9 peptide to nuclei or to live cells (Figs. 3B, C, 6B, C and 7A, B; Suppl. Figs. 16, 17 and 25A–F), suggesting that the topographic differences in the nuclei containing the full-length or Δ C forms are the direct result of altered structure and functioning of the histone variant, rather than secondary, e.g., compensatory, consequences thereof developing in the cells expressing the truncated variant. Although differential masking/unmasking or changed accessibility of ZAbA- or ZAbB-binding epitopes in the different nuclear compartments may also contribute to the altered nuclear landscape, reorganization of chromatin upon C9 treatment was observed also through the spectacles of DNA staining (Fig. 3J) as well as in the case of Flag-tagged H2A.Z (Suppl. Fig. 18).

Based on recent cryo-EM analyses⁴⁶, a H2A motif coined “regulating-octamer-folding” (ROF) plays an important role in nucleosome stability, interacting with the N-terminal H3 helix. This motif, residing between amino acids 106–111, is present both in H2A and H2A.Z.1. In the alternatively spliced variant H2A Z2.2, it is replaced by a non-canonical ROF and the terminal 14 amino acids are also missing as compared with H2A.Z.1. The destabilized nature of H2A.Z.2.2 containing nucleosomes, not investigated in our work, was attributed primarily to the disruptive effect of the noncanonical ROF in ref. 46. The contribution to stability of the last 14 amino acids missing from H2A.Z.1 was not possible to judge, since this segment (encompassing the noncanonical ROF) was invisible in cryo-EM. Based on the efficient modulation of nucleosome stability with added C9, the contribution of the C-terminal tail to overall nucleosome stability may be very significant. According to another recent cryo-EM study²¹, the H2A.Z-containing mononucleosomes formed on the Widom 601 sequence are less stable than those containing canonical H2A, a feature determined by the last 6 amino acids of its unstructured C-terminal tail, while the variant histone-containing nucleosome arrays assume a more regular and condensed state. Whether interactions between the enlarged acidic patch of the H2A.Z nucleosome and the H4 tail of the neighboring nucleosome described previously, or interactions involving the C-terminal tail, or both explain the more condensed state of the H2A.Z-containing chromatin fibers, have not been determined.

In view of the data presented, the tail may mediate interactions between neighboring chromatin fibers, increasing the stability of the nucleosomes connected. When this engagement is thwarted by reader protein binding, tail truncation or masking by a tag, the stability features of canonical nucleosomes prevail. Tethering of peripheral

heterochromatin to the lamina, perhaps involving H2A.Z^{lmm}, could also account for the tail-dependence of increased stability of the nucleosomes involved. As a third alternative, the C-terminal tail could engage with a binding site within the same nucleosome rendering the variant histone more resistant to salt-induced dissociation; in this case the intranuclear localization and stability of H2A.Z-nucleosomes would not be directly linked. For a further, more complex scenario, and discussion of differences between the *in vitro*, cryo-EM data and those of the *in situ* elution experiments, see Suppl. Discussion.

The stability of H2A.Z nucleosomes appear not to be directly affected by isotype specific features, PTMs and binding of PWWP2A

PTMs targeting the C-terminal region of H2A.Z⁵⁷ were considered as potential determinants of nucleosomal stability features. However, at least certain PTMs appear not to play a primary role in the case of H2A.Z containing nucleosomes (Suppl. Fig. 2I–L). This conclusion applies also to acetylation since we did not see any significant shift in the affinity of H2A.Z binding to nucleosomes when the global extent of histone acetylation was increased by treatment with HDAC inhibitors or when a non-acetylatable H2A.Z mutant was expressed in the cells (Suppl. Fig. 2I, L). The observation that the antibody supposed to be specific for acetylated H2A.Z⁵⁸ behaves as ZAbA (Suppl. Fig. 2L) is due to the fact that it readily recognizes the non-acetylated H2A.Z of the 5KR cells devoid of N-terminal acetylations; the H2A.Z-specificity of this antibody was verified in the silencing experiment shown in panel of Suppl. Fig. 5E.

Reader proteins such as PWWP2A⁵⁹, as well as chaperones/remodelers^{47,59} can bind to the H2A.Z C-terminus, raising the possibility that binding of these factors to H2A.Z can modulate the stability of H2A.Z containing nucleosomes. PWWP2A apparently does not contribute to the unusually high stability of the ZAbA detected H2A.Z-nucleosomes in our assay conditions, since it dissociates from the chromatin already at low salt (Suppl. Fig. 3A–C). *In vivo*, however, binding of this or any of the other readers may prevent the C-terminal tail from engaging in other intermolecular interactions.

According to the H2A-like elution profiles of fluorescent protein-tagged H2A.Z.1 and Z2 (Suppl. Fig. 4A), the two tagged hypervariants may not differ significantly in their stability features at euchromatic locations. However, given that the elution curves, reflecting the nucleus-averaged stability of all H2A.Z species present, depend on even small tags, especially on their C-terminus (Suppl. Fig. 4F), it becomes difficult to make a comparison based on data obtained with tagged histones. Similar observations on the influence of tags have been reported on the Flag tag-dependent molecular interactions involving H2B⁶⁰. Thus, potential differences in the stability features of H2A.Z.1 and H2A.Z.2.1 could not be assessed based on the elution characteristics of the tagged hypervariants. However, expression of either hypervariant on a DKO background made such a comparison possible (Suppl. Fig. 2A), and have yielded negative results. In summary, the above negative data are in line with the finding that *in vitro* reconstituted nucleosomes are also stable (Fig. 1G) in line with ref. 39. This observation is in line with a model where the higher stability is the primary feature of H2A.Z-nucleosomes when assessed *in situ*, unless or until the inter- or intranucleosomal links, and laminar tethering mediated by the C-terminal tail are overridden by competing molecular associations.

The tail peptide binds to reconstituted nucleosomes

Nucleosome stability is assessed routinely by exposing them to challenging conditions like elevated salt concentration, which may itself perturb the structure. However, we observed entirely different elution characteristics for ZAbA- and ZAbB-detected, and tagged histone containing nucleosomes using the same salt concentration series; furthermore, salt resistance of the nucleosomes recognized by ZAbA

was reverted upon nicking treatment. Thus, the stability features observed in the elution experiments are just revealed by, and are not the consequence of, the salt treatment. On the other hand, the nucleosomal binding of the labeled C9 peptide was enhanced to ~90 nM in the presence of 700 mM salt, while DNA binding was unaffected (Fig. 5); this ionic strength favors loss of the histone dimers according to high precision FRET studies⁵². A more open, nucleosomal structure, experimentally induced in the canonical nucleosomes by salt, could accommodate the C-terminal tail of a juxtaposed H2A.Z nucleosome. The tail of the histone variant is likely to protrude out of the nucleosome so as to be able to reach a binding site in a neighboring chromatin fiber^{61,62}. The relaxed state of plasmid DNA in the reconstituted nucleosomal arrays of our hydroxyapatite experiments (see “Methods”; Fig. 1G) could also allow such interactions to occur between nucleosomes residing on the same plasmid and explain increased salt-resistance. On the other hand, an interpretation based on the possible interaction of the tail with a binding site formed within the same nucleosome with consequential strengthening of molecular cohesion and stability would also be compatible with our salt elution data. In this latter scenario, the increased stability of H2A.Z nucleosome arrays would be unrelated to the H2A.Z tail and could involve the acidic patch, as suggested²¹.

As Suppl. Fig. 22 demonstrates, about 12% of the peptide was found in the slower fraction representing C9-CF bound to nucleosomes prepared from recombinant histones and the 147 bp long Widom 601 core sequence⁶³, while the slow component was undetected in the case of the labeled scrambled peptide. Based on this value, the K_d of C9 binding to these nucleosomes is ~320 nM (calculated as in ref. 51). Weaker association (K_d ~ 2 μ M) was obtained for nucleosomes containing longer (170 bp) DNA (Fig. 5). K_d values in the range of 1 nM to ≥ 1 μ M measured for the binding of various H3K4-modified peptides to purified nucleosomes have been considered physiologically relevant⁶⁴. This relatively weak binding, as measured at low salt conditions, may be sufficient to support the formation of a condensed superstructure from juxtaposed nucleosomes; however, it could also be antagonized *in vivo* by structural components of the chromatin like H1 and HMGB1, with K_d values for DNA binding in the low micromolar range⁶⁵, washed out from the nuclei in the elution assay conditions. At low salt, the affinity of the tail to nucleosomes and DNA were also similar (Fig. 5), suggesting that it is the internucleosomal linker DNA that primarily engages with the tail in these conditions. Consolidation of the interaction to K_d = 90 nM at 700 mM salt was not observed in the case of pure DNA, so C9-CF may bind to the nucleosome core in these ionic strength conditions.

C9-CF-binding to H2A.Z-nucleosomes exceeded its binding to canonical nucleosomes at low ionic strength (Suppl. Fig. 22). It remains to be investigated how elevated salt concentrations influence this difference, to what extent C9 binds to the nucleosome core and to the linker DNA, how this binding depends on the length of the DNA containing the nucleosome positioning sequence and on the species origin of the histones. The possibility that the tail peptide may bind to DNA in a superhelicity dependent fashion, and may also influence it, is also yet to be investigated. With these limitations, our FCS measurements support the possibility that binding of the H2A.Z C-terminal tail to nucleosomal components within the same nucleosome or mediating nucleosome-nucleosome contacts is a key factor in determining nucleosome stability and establish the experimental platform for further biophysical studies. Binding of C9 to reconstituted nucleosomes (in the absence of PTMs) is in agreement with the genome-wide effects of the peptide when added to nuclei (Figs. 3 and 4).

Global chromatin accessibility features are affected by interactions involving the H2A.Z tail

The parallel sensitization of chromatin to nickase, MNase, and DNase I in H2A.Z Δ C-expressor DKO DT40 nuclei (Fig. 2E–G, Suppl. Fig. 13A)

suggests that access to DNA rather than the exonucleolytic digestion subsequent to the initial nicking is the rate-limiting step in MNase digestion. The relaxation of internucleosomal superhelicity upon the initial single-strand cleavages significantly contributes to nucleosome destabilization^{36,66}, rendering the entire chromatin loop more open to further cleavages, amplifying and extending the effect of the treatment.

The remarkable differences in overall nuclease sensitivity between the full-length H2A.Z.1-expressor and H2A.Z Δ C-expressor DKO DT40 nuclei (Fig. 2) may reflect the altered contribution to what is measured over the entire nucleus by the dispersed peripheral heterochromatin, and may also reflect alterations in the dynamics of the euchromatic H2A.Z; indeed, these nucleosomes exhibit remarkable heterogeneity in terms of accessibility features of the DNA packaged²³. The nucleosomes of euchromatin comprise a relatively minor fraction of the total chromatin, and even spreading of destabilization upon the initial nicking via superhelical relaxation to the whole loop⁶⁶ may not account for the increment of MNase sensitivity detected on a global level in Δ C vs. full-length H2A.Z.1-expressor DT40 DKO cells (or upon C9 treatment of HeLa nuclei; Fig. 3).

On the other hand, loss of laminar anchorage or decondensation of the peripheral heterochromatin may also alter internucleosomal superhelicity what could lead to nucleosome destabilization involving the entire chromatin loop⁶⁶. This interpretation is in line with the possible tail-dependence of loop anchorage (Suppl. Fig. 12) and the difference between the effect of nicking in DT40 harboring full-length or truncated H2A.Z1 (Suppl. Fig. 8D).

In HeLa nuclei, the C9 treatment-enhanced release of a number of proteins of its euchromatic interactome by MNase (Suppl. Table 4) reveals that accessibility of DNA flanking H2A.Z-nucleosomes binding these molecular complexes is C9-sensitive in euchromatin. These DNA regions, however, comprise only a fraction of the total DNA content, not accounting for the overall increments in digestability by various nucleases and by MNase at typical euchromatic and heterochromatic regions (Fig. 3G, H). The CUT&RUN data (Fig. 4, Suppl. Fig. 19) and comparison of the sequencing read distributions between the C9 treated and untreated samples (Suppl. Fig. 21) suggest that the peptide facilitated access of nucleases to chromatinized DNA genome-wide. Given the magnitude of C9-induced sensitization to MNase, any possible major regional preference of this effect would have likely been detected in our assays. C9 treatment of HeLa nuclei in isotonic salt conditions did not lead to eviction of either canonical or H2A.Z-containing nucleosomes (Suppl. Fig. 17A, B); thus, the C9-induced increment in accessibility of a large fraction of genomic DNA to nucleases was due to the decreased protection of the DNA wrapped around them, from nucleases, rather than to a loss of nucleosomes. This interpretation is in line with the fact that resistance of nucleosomes to salt and to nucleases strongly correlate in all the experimental scenarios explored.

H2A.Z tail-dependence of gene expression and the possibility of epigenetic modulation

In the DT40 experimental system, perhaps due to the adaptation of the cells to their tailless histone variant, the differences in gene expression were not extensive (especially in the case of Δ C vs. DKO H2A.Z.1; Suppl. Fig. 14, Suppl. Table 3), in spite of the global contribution of H2A.Z to gene expression regulation³⁷, and with the massive differences in chromatin structure both in terms of H2A.Z nuclear localization and accessibility features (Figs. 2 and 3). Nonetheless, these differences have functional consequences as shown by the altered DNA damage response (DDR; Suppl. Fig. 15). The architectural changes exhibited by DKO H2A.Z Δ C chromatin relative to full-length histone expressing cells, and the increased sensitivity of these cells to etoposide and doxorubicin (Suppl. Fig. 15) are closely reminiscent of the dramatic influence of H2A.Z on resistance to genotoxic stress in *Saccharomyces cerevisiae*⁶⁷. For further possible connections of the gene expression changes to DDR, see Supplementary Discussion.

The C9 peptide could be efficiently introduced into live HeLa and melanoma cells. Changes in gene expression could be primarily accounted for by modulation of euchromatin. On the other hand, alterations of constitutive, mostly peripheral heterochromatin, which comprises up to 40% of the *human* genome, could be relevant in the context of aging, various neurological disorders, and carcinogenesis⁶⁸. The rearrangement of peripheral heterochromatin upon treatment of nuclei as well as of live cells with C9 demonstrates that global features of heterochromatin are amenable to modulation by the peptide. The CUT&RUN/MS data showing that the linker and/or nucleosome-free DNA around the H2A.Z containing nucleosomes become readily accessible to MNase upon C9 treatment (Suppl. Table 4) directly demonstrate that euchromatic molecular complexes of H2A.Z can also be readily modulated by the peptide. Indeed, introduction of the peptide into live cells leads to down-regulation of a cohort of genes (Fig. 7C), in line with the large number of genes found to be H2A.Z-regulated (ref. 127 in ref. 34). Certain pathways are overrepresented among the down-regulated genes (Fig. 7L), so the effect cannot be due to nonspecific transcriptional suppression or cytotoxicity, also in view of the fact that the continuously growing cells showed no loss of viability (Suppl. Fig. 24). Intriguingly, the down-regulated genes themselves are exclusively localized outside the Giemsa-dark bands (Fig. 7E) containing late-replicating DNA⁶⁹. Thus, although H2A.Z is deposited all over the chromosomes (Fig. 7H), expression-determining interactions of its C-terminal tail appear to be limited to genes residing outside the late-replicating domains, raising the possibility of an intriguing connection between activation of early replication origins by H2A.Z⁷⁰ and tail-dependent transcriptional regulation involving the variant histone. Alternatively, since the Giemsa bands can be distinguished also by staining with intercalating dyes⁷¹, the binding of which is highly sensitive to superhelical constraint⁶⁶, differential binding of C9 to the DNA comprised by the different bands might explain the band localization of the down-regulated genes. This scenario would be supported if C9 could distinguish between supercoiled and relaxed DNA, a possibility not yet explored. The cellular states compatible with or required for the effect of C9 on gene expression are also yet to be characterized. Whether and how modulation of gene expression may be related to the changes in chromatin architecture has not been established, what will be important considering the recent identification of cytoplasmic ANP32e-H2A.Z interactions of regulatory significance⁷².

In summary, the C-terminal H2A.Z tail can impact chromatin at each level of its organization, from nucleosome to chromosome bands, and the enigmatic involvement of H2A.Z in both gene activating and silencing processes appears to be determined to a great part by the molecular interactions involving its unstructured C-terminal tail. We propose that the tail may be bound to the nucleosome core or internucleosomal DNA, increasing nucleosome stability via engagement of the tail within the same nucleosome or by promoting chromatin condensation. Alternatively, the tail could bind reader proteins/chaperones/remodelers, preventing this engagement. A high salt-resistant fraction of H2A.Z was detected in the nuclear lamina, which may play a role in the tethering of heterochromatin. The alternative engagements of the tail affect the stability and landscape of H2A.Z-nucleosomes, global chromatin accessibility features in both euchromatin and heterochromatin, with possible consequences on gene expression. Further investigation of this remarkable example of epigenetic modulation is warranted also in the hope that the C9 effect may be exploited to modulate different cellular states under H2A.Z control.

Methods

Chemicals, peptides

All reagents were from Sigma-Aldrich (St. Louis, Missouri, USA) unless otherwise stated. Fmoc-Rink Amide MBHA resin and all amino acid derivatives used in this study were purchased from Iris Biotech GmbH

(Marktredwitz, Germany). Peptides of different lengths, corresponding to the C-terminus of H2A.Z were synthesized manually on 2CTC resin (0.6 mmol/g loading capacity) following standard Fmoc/Bu strategy using the in situ DIC/HOBt coupling method. The complete sequences were removed from the resin with 10 ml of cleavage mixture (95% TFA, 2.5% triisopropylsilane (TIS), 2.5% H₂O), stirred for 1.5 h at RT. The crude products were precipitated in ice cold MTBE (methyl-tert-butyl ether) and centrifuged for 4 min at 2500 × *g*. After washing three times with MTBE, the crude products were dissolved in water and the solution was purified by RP-HPLC and lyophilized.

The fluorescent peptide derivative of C9 was prepared similarly but was elongated on the C-terminus with an aminohexane (Ahx) group and a lysine. The peptide was labeled on resin, via coupling the lysine's ε-amino group with 5(6)carboxy-fluorescein (CF), which resulted the peptide H-GKKGQKTV-Ahx-K(CF)-OH. 'Scrambled' reference peptide (SCR), used as a negative control, was generated by random shuffling of amino acids. The generated sequence was checked against Uniprot KB database. This was repeated until a peptide sequence not showing match with the database was found. The resulting control peptide was: H-KQGTGKVQK-OH.

Plasmids

The plasmids carrying different isoforms of the histone variant H2A.Z (provided by Juan Ausio) were transformed into *Escherichia coli* DH5α by heat shock and selected on LB plates containing 100 μg/ml kanamycin.

Cells

HeLa, H2B-GFP expressor HeLa, H3-GFP expressor HeLa⁷³ (provided by Hiroshi Kimura, Yokohama, Japan), GFP-H2A.Z expressor HeLa (provided by H. T. Marc Timmers), 293T and MEL1617 cells (from Coriell Institute for Medical Research) were cultured in DMEM supplemented with 10% FCS, 2 mM L-glutamine, 100 μg/ml streptomycin, 100 U/ml penicillin. WM35 cells (Coriell Institute for Medical Research) were cultured in RPMI supplemented with 10% FCS, 2 mM L-glutamine, 100 μg/ml streptomycin, 100 U/ml penicillin. Wild type, H2A.Z.1 knock-out, H2A.Z.2.1 knock-out and mutant (SKR and ΔC) H2A.Z.1 expressing double knock-out DT-40 chicken B cells (provided by Masahiko Harata^{37,38}) were cultured in DMEM supplemented with 2% chicken serum, 8% FCS, 2 mM L-glutamine, 100 μg/ml streptomycin, 100 U/ml penicillin.

Embedding live cells into low melting point agarose

Prior to embedding, 8-well microscope chambers (Ibidi, Martinsried, Germany) were coated with 1% (m/v) low melting point (LMP) agarose. 150 μl liquid agarose diluted in distilled water was dispensed into each well and was immediately removed so that a thin agarose layer remained on the surfaces and was left to polymerize on ice for 2 min, then kept at 37 °C until the surface of the wells dried out. This coating procedure was repeated once more on the same chambers. Embedding was performed keeping cells and agarose at 37 °C. The cell suspension containing 6×10^6 cells/ml was mixed with 1% LMP agarose diluted in PBS at a v/v ratio of 1:3. 22 μl of the cell-agarose suspension was dispensed in the middle of the wells and the chambers were covered with home-made rectangular plastic coverslips cut out from a 200-μm thick, medium weight polyvinyl chloride binding cover (Fellowes, Inc., Itasca, Illinois, USA). Cells were left to sediment on the surface of the coated wells for 4 min at 37 °C, then kept on ice for 2 min. After polymerization of the agarose, 300 μl ice cold complete culture medium was added to each well, a step aiding removal of the coverslips.

Preparation of nuclei/permeabilization, histone eviction by salt, nuclear halos

The agarose embedded cells at the bottom of the wells were washed with 500 μl ice cold PBS, 3 times for 3 min each, then permeabilized

with 500 μ l ice cold 1% (v/v) Triton X-100 dissolved in PBS/EDTA (5 mM EDTA in PBS), for 10 min. This step was repeated once more. After permeabilization, nuclei were washed with 500 μ l ice cold PBS/EDTA 3 times for 3 min and were treated with different concentrations of NaCl or intercalator solutions on ice. Nuclei were incubated with 500 μ l of ice cold salt or intercalator solution for 60 min. At this point nuclear halo samples were prepared by adding 2 M NaCl dissolved in PBS/EDTA to the nuclei for 60 min on ice (neutral halos). After this treatment, nuclei were washed with 500 μ l ice cold PBS/EDTA 3 times for 3 min. Since NaCl was diluted in PBS/EDTA, the salt concentrations indicated on the X axes of the graphs in all the figures show the total NaCl concentrations together with NaCl present in the PBS buffer. For the analysis of the curves SigmaPlot 12.0 software was applied, using either the 'Sigmoid 3 parameter' (in the case of linear plots) or 'Standard curves: Four Parameter Logistic Curve' (in the case of logarithmic plots) curve-fitting subroutines. Elution curves were 'normalized to 0' by subtracting the smallest fluorescence intensity value from all the others, unless stated otherwise, and to '1' by dividing the mean fluorescence intensities represented by the datapoints by that of the nontreated sample. The number of analyzed G1 nuclei was between 200 and 2000/well, out of the about 500–5000 cells scanned. All the SEM values indicated in the figures were calculated from the datapoints of the cell population analyzed in the given experiment.

Peptide treatment of permeabilized nuclei

The synthetic peptides were used at a final concentration of 30 μ M, dissolved in PBS/EDTA/1%BSA. 200 μ l of peptide solution/well was applied and nuclei were incubated with the peptide overnight at 4 °C. After incubation, the peptide solution was washed out with 500 μ l ice cold PBS/EDTA 3 times.

Introduction of peptides into live cells

0.5 \times 10⁶ HeLa or MEL1617 melanoma cells were placed in a 35 mm cell culture Petri dish and grown overnight before peptide treatment. Cyclodextrin/peptide complex formation was performed by mixing 30 μ M peptide and 300 μ M SBECD (Sulfobutylether- β -Cyclodextrin; CycloLab, Budapest, Hungary) diluted in colorless, serum-free RPMI1640 and incubated for 1 h at room temperature. 2 ml SBECD/peptide complex was added to the cells and incubated for 2 h at 37 °C in 5% CO₂ atmosphere. After incubation, cells were washed with complete RPMI medium once and further cultured overnight before agarose embedding.

Immunofluorescence labeling

After salt or intercalator treatment the samples were incubated with 500 μ l 5% (m/v) Blotto Non-Fat Dry Milk (Santa Cruz Biotechnology Inc., Santa Cruz, California, USA) in PBS/EDTA for 30 min on ice, to decrease nonspecific binding of the antibodies. The blocking solution was washed out with 500 μ l ice cold PBS/EDTA 3 times for 3 min and indirect IF labeling was performed using rabbit polyclonal anti-H2A.Z (ab97966 (ZAbA), lot num.: GR90761-2, GR90761-6, GR90761-8, GR90761-12, GR90761-13, GR90761-15, ab4174, lot num.: 1015872-1, 1058382-2, Abcam, Cambridge, UK; 1 mg/ml), sheep polyclonal anti-H2A.Z (acetyl K4 + K7 + K11, ab18262, lot num.: GR306397-1, Abcam, Cambridge, UK; 0.5 mg/ml), rabbit polyclonal anti-H2A.Z (PA5-17336 (ZAbB), lot num.: VH3053562, XK3767973, UB2712502, VC2958177, Thermo Fisher Scientific, Waltham, Massachusetts, USA; 62 μ g/ml), rabbit polyclonal anti-H2A.Z (07-594, lot num.: 3946459, Merck-Millipore, Darmstadt, Germany), rabbit polyclonal anti-PWWP2A (NBP2-13833, lot num.: A106444, Novus Biologicals, Centennial, Colorado, USA; 0.2 mg/ml), rabbit polyclonal anti-H2A.X (ab11175, Abcam, Cambridge, UK; 1 mg/ml), rabbit polyclonal anti-H2A (ab18255, lot num.: GR3211735-2, Abcam, Cambridge, UK; 1 mg/ml), rabbit polyclonal anti-H2B (ab52484, lot num.: GR3232535-3, GR3173752-4, GR163233-5,

Abcam, Cambridge, UK; 1 mg/ml), *mouse* monoclonal anti-H1 (ab71594, clone name: AE-4, lot num.: GR159309-23, Abcam, Cambridge, UK; 1 mg/ml), *mouse* monoclonal anti-HP1 (ab234085, clone name: 3A11F8, lot num.: GR3241506-8, Abcam, Cambridge, UK; 1 mg/ml), rabbit polyclonal anti-Lamin B1 (ab16048, lot num.: GR3188003-1, Abcam, Cambridge, UK; 0.1–1 mg/ml), rabbit polyclonal anti-Rad21 (ab992, lot num.: GR-3235714-1, Abcam, Cambridge, UK; 0.2–1 mg/ml), rabbit polyclonal anti-CTCF (ab70303, lot num.: GR3218438-2, Abcam, Cambridge, UK; 0.2 mg/ml) *mouse* monoclonal anti- γ H2A.X (05-636, clone name: JBW301, Merck-Millipore, Darmstadt, Germany), *mouse* monoclonal anti-H3K4me3 (ref. 74; clone name: CMA304, lot num.: 16H10, 0.5 mg/ml), rabbit polyclonal anti-H3K9me3 (ab8889, lot num.: 699686, Abcam, Cambridge, UK; 0.2–1 mg/ml) *mouse* monoclonal anti-H3K9me3 (ref. 74; clone name: CMA318, lot num.: 2F3 0.5 mg/ml) or *mouse* monoclonal anti-H3K27me3 (ref. 75; clone name: CMA323, lot num.: 1E7 0.5 mg/ml) primary antibodies, all diluted in 150 μ l of PBS/EDTA/1% BSA (PBS/EDTA supplemented with 1% w/v bovine serum albumin), at 4 °C, overnight. All the above antibodies were applied to the wells at a titer of 1:800. After labeling with the primary antibodies, the nuclei were washed with 500 μ l ice cold PBS/EDTA 3 times for 10 min. Labeling with the secondary antibodies was performed in 150 μ l PBS/EDTA for 2 h on ice, using Alexa fluor 488 (A488) or Alexa fluor 647 (A647) conjugated goat anti-mouse IgG or goat anti-rabbit IgG antibodies (Thermo Fisher Scientific, Waltham, Massachusetts, USA; 2 mg/ml). In the case of sheep polyclonal anti-H2A.Z (acetyl K4 + K7 + K11, ab18262) Alexa fluor 633 (A633) conjugated goat anti-sheep IgG (Thermo Fisher Scientific, Waltham, Massachusetts, USA; 2 mg/ml) secondary antibody was used. The secondary antibodies were also used at a titer of 1:800, diluted in PBS/EDTA from 2 mg/ml stock solutions. After labeling with the secondary antibodies the agarose embedded nuclei were washed with 500 μ l ice cold PBS/EDTA 3 times, for 10 min. Then the samples were fixed in 1% formaldehyde (dissolved in PBS/EDTA) at 4 °C, overnight. After fixation the wells containing the embedded nuclei were washed with 500 μ l ice cold PBS/EDTA 3 times for 3 min and were stained with 200 μ l of 12.5 μ g/ml propidium-iodide (PI, dissolved in PBS/EDTA) for 30 min, on ice. The stained nuclei were washed 3 times with 500 μ l ice cold PBS/EDTA for 3 min. Fluorescence intensity distributions were recorded using an iCys laser scanning cytometer (LSC), as described below.

Western blot

200 ng of H2A.Z.1, H2A.Z.2, H2A (H2042, Sigma-Aldrich, St. Louis, Missouri, USA; 1 mg/ml) and H2B (H2167, Sigma-Aldrich, St. Louis, Missouri, USA; 1 mg/ml) histones were separated on a 12% SDS-polyacrylamide gel and electro-blotted onto a 0.45- μ m pore size PVDF membrane. The blot was saturated with milk blocking buffer (5% milk power/0.2% Tween-20/PBS) for 1 h and then labeled by ZAbA or ZAbB. Both were applied at a final concentration of 0.4 μ g/ml in 1:2500 dilution in milk blocking buffer overnight at 4 °C. After washing with 0.2% Tween-20/PBS for 6 \times 5 min, the membrane was incubated with goat-anti-mouse IgG secondary antibody conjugated with horseradish peroxidase (ab6789, Abcam, Cambridge, UK; 2 mg/ml) at a final concentration of 0.8 μ g/ml/in 1:2500 dilution in milk blocking buffer for 1.5 h at room temperature. After washing with 0.2% Tween-20/PBS for 6 \times 5 min, the bands were visualized with SuperSignal™ West Pico PLUS Chemiluminescent Substrate (Thermo Fisher Scientific, Waltham, MA). The signal was detected by chemiluminescence using the FluorChem Q gel documentation system (Alpha Innotech Corp., San Leandro, CA).

Etoposide treatment

Agarose embedded live cells were treated with etoposide (TEVA, Debrecen, Hungary) used at a final concentration of 25 μ M. The drug was diluted in 300 μ l complete DMEM medium and the cells were incubated together with the drug at 37 °C in 5% CO₂ atmosphere.

Laser scanning cytometry (LSC)

Automated microscopic imaging was performed using an iCys instrument (iCys[®] Research Imaging Cytometer; CompuCyte, Westwood, Massachusetts, USA). Green fluorescent protein (GFP), SYBR Gold, A488 and PI were excited using a 488 nm Argon ion laser, A647 with a 633 nm HeNe laser. Fluorescence signals were collected via an UPlan FI 20× (NA 0.5) objective, scanning each field with a step size of 1.5 μm. GFP and A488 were detected through 510/21 nm and 530/30 nm filters, respectively, while A647 and PI were detected through a 650/LP nm filter.

Data evaluation and hardware control were performed with the iCys 7.0 software for Windows XP. Gating of G1 phase cells was according to the fluorescence intensity distribution of the DNA labeled with PI or SYBR Gold. In order to scan similar numbers of cells per sample in the field set, the same number of cells were embedded in the different samples.

Confocal laser scanning microscopy (CLSM)

Confocal images were taken using an FLUOVIEW FV 1000 confocal microscope (Olympus, Center Valley, Pennsylvania, USA) based on an inverted IX-81 stand with an UPLS APO 60× (NA 1.35) oil immersion objective. GFP or A488 were excited by a 488 nm Argon ion laser. A647 and PI were excited by a 633 nm and 543 nm HeNe laser, respectively.

Colocalization and texture analysis

For image and texture analyses, the Just Another Colocalization Plugin of the Image J software (<http://imagej.nih.gov/ij/>) and the Measure-Granularity module of the CellProfiler 2.2.0 software, respectively, were used. For colocalization measurements Manders colocalization coefficient (MCC) representing the fraction of overlapping pixels was calculated in Image J.

MNase, nickase, and DNase I treatment

Live cells were embedded into agarose as described above and treated with 500 μl ice cold lysis buffer (0.4% (v/v) Triton X-100, 300 mM NaCl, 1 mM EDTA, 10 mM Tris-HCl, pH 8.0) for 10 min, followed by treatment with 500 μl ice cold 1% (v/v) Triton X-100 dissolved in PBS/EDTA, for 10 min, then washed 3 times with 500 μl ice cold PBS/EDTA. MNase, the frequent cutter Nt.CviPII nickase (recognition site: CCD; New England Biolabs Inc., Ipswich, Massachusetts, USA) and DNase I were applied after the washing steps following permeabilization. Where indicated, the permeabilized and washed nuclei were incubated with the peptides (C9 or SCR) overnight at 4 °C, and the peptides were washed out before nuclease addition. Before digestion, the samples were equilibrated with MNase buffer (1 mM CaCl₂, 50 mM Tris-HCl pH 7.5), nickase buffer (10 mM Tris-HCl pH 8.0, 50 mM NaCl, 10 mM MgCl₂, 1 mg/ml BSA) or with DNase I buffer (10 mM Tris-HCl pH 8.0, 0.1 mM CaCl₂, 2.5 mM MgCl₂) by washing 3 times with 500 μl of the buffer solutions. Nickase treatment was performed in 300 μl nickase buffer for 30 min at 37 °C, using the enzyme at a final concentration of 0.5 U/ml. MNase and DNase I digestion were performed in 300 μl MNase, or DNase I buffer for 10 min at 37 °C, at a final concentrations indicated on the figures. After enzymatic treatments, the samples were washed with 500 μl ice cold PBS/EDTA 3 times for 3 min.

Microarray experiments

For microarray analyses, Cyanine3 (Cy3) labeled cRNA was prepared from 0.1 μg Total RNA using the Low Input Quick Amp Labeling Kit (Agilent Technologies) according to the manufacturer's instructions, followed by RNeasy column purification (QIAGEN). For methodical details of the Agilent platform used, see Supplementary Methods.

RNA-Seq and pathway analysis

To obtain global transcriptome data high throughput mRNA sequencing analysis was performed on the Illumina sequencing platform.

MEL1617 cells were grown in 6-well plates and treated with C9 or SCR for 2 h (see details above). The three biological replicates of the RNA-seq experiments have been prepared/processed on the same day to reduce spontaneous fluctuations of the expression profile. Total RNA was isolated from 1 million cells/sample using GenElute Mammalian Total RNA Miniprep Kit (Sigma) according to the manufacturer's instructions. RNA sample quality was checked on Agilent BioAnalyser using Eukaryotic Total RNA Nano Kit according to manufacturer's protocol. Samples with RNA integrity number (RIN) value >7 were accepted for the library preparation process. For details of the preparation of RNA-Seq libraries, amplification and sequencing on an Illumina platform, see Supplementary Methods. For the steps of further sample processing and bioinformatic analyses of the fastq data, see Supplementary Methods.

Whole-genome sequencing for comparative mapping of MNase sensitivity before and after C9 treatment

HeLa cells were embedded into agarose in the wells of 8-well Ibidi chambers and permeabilized as described above. Different chambers were prepared parallel for LSC measurement (to measure the effect of the peptide on the overall degree of MNase digestion) and for whole-genome sequencing. After peptide treatment, nuclei were digested with 10⁻³ U/ml MNase as described above. After enzymatic treatment, nuclei were washed with 500 μl ice cold 1×PBS/EDTA 3 times for 3 min, followed by fixation with 4% formaldehyde for 10 min, on ice. After fixation, samples were washed with 500 μl ice cold 1×PBS/EDTA 3 times, for 3 min each. For LSC measurement, the samples were stained with 200 μl 1×SYBRGold diluted in PBS/EDTA, on ice for 30 min, then washed with 500 μl ice cold 1×PBS/EDTA 3 times before LSC scanning. For whole-genome sequencing, agarose embedded cells were scraped and removed from the wells. 12 wells of CTRL, CTR(MN), C9 or C9(MN) were pooled resulting in 400 μl samples. These were melted up to 70 °C for 10 min, then cooled down to 42 °C and digested with 4 U of agarase enzyme/400 μl sample (Thermo Fisher Scientific, Waltham, Massachusetts, USA) for 30 min. Samples were further digested with 40 μg/400 μl proteinase K (Thermo Fisher Scientific, Waltham, Massachusetts, USA) overnight at 55 °C. After digestion, DNA was sheared by sonication using a Diagenode Bioruptor instrument (Diagenode, Liège, Belgium) to generate ≈250 bp fragments, that were purified (MinElute PCR Purification Kit; Qiagen Inc., Valencia, California, USA) and stored at -70 °C until sequencing.

After shearing, size selection was performed to enrich for -280 bp DNA fragments using DNA Clean Beads (MGI, Shenzhen, China). The sequencing library was generated using MGIEasy Universal DNA Library Prep Set (MGI) according to the manufacturer's protocol. Briefly, the size selected DNA fragments went through end repair, A-tailing, adapter ligation, and amplification steps. The ds library fragments were circularized and one of the strands was digested. Circularized single-stranded fragments were used for generating DNA nano balls (DNB) by rolling circle amplification. DNB sequencing was performed on a MGI DNBSEQ GS-400 instrument (MGI), to yield paired-end, -150 bp long sequencing reads. Library preparation, sequencing, and primary data analysis were performed at the Genomic Medicine and Bioinformatics Core Facility of the University of Debrecen, Hungary.

Analyses of the Whole Genome Sequencing data was performed on the Galaxy platform (EU server: usegalaxy.eu)⁷⁶. For details of quality control, mapping of the reads to the reference genome, calculations related to read coverages, specification of the peak-sets download from ENCODE, see Supplementary Methods.

Sample preparation for mass spectrometric (MS) measurements of the salt-resistant fraction of nuclear proteins

80 × 10⁶ H3-GFP expressing HeLa cells in 2.5 ml cell culture medium were mixed with an equal amount of 1% LMP diluted in PBS. Agarose

blocks were prepared where each blocks contained 90 μ l of agarose/cell suspension. The blocks were washed 3 times in 15 ml 1 \times PBS for 10 min. Permeabilization of cells was performed in ice cold 15 ml 1% Triton X-100 diluted in PBS/EDTA, twice for 30 min. Blocks were washed 5 times in 15 ml PBS/EDTA. Blocks were treated with 15 ml EBr diluted in PBS/EDTA/600 mM NaCl at a concentration of 100 μ g/ml, or with 15 ml 1.2 M NaCl solution diluted in PBS/EDTA, for 60 min. Blocks were washed 3 times in 15 ml PBS/EDTA for 20 min and the proteins that remained in the nuclei were eluted with 15 ml of 2 M NaCl diluted in PBS/EDTA for 60 min. All the washing steps were performed using ice cold solutions. Eluted proteins were concentrated using a 10 K Amicon tube (Merck-Millipore, Darmstadt, Germany) and the buffer was changed to PBS. Proteins were eluted from the filter with 250 μ l PBS and stored at -20°C for MS analyses. For details of sample processing, Orbitrap MS analyses and protein identification, see Supplementary Methods.

LC-MS/MS analyses of salt-eluted nuclear samples

The samples were digested in-solution with trypsin. Before digestion, samples were reduced using 10 mM dithiothreitol for 1 h at 56°C , followed by alkylation with 20 mM iodoacetamide for 45 min. Overnight trypsin digestion was carried out using stabilized MS grade bovine trypsin (Sciex, Framingham, MA, USA) at 37°C . The reaction was stopped by adding concentrated formic acid and the digests were desalted using C18 Pierce tips (ThermoScientific, Waltham, MA, USA) according to the manufacturer's protocol. The desalted peptides were dried and re-dissolved in 10 μ l 1% formic acid. Before MS analysis the peptides were separated using a 180 min water-acetonitrile gradient at 300 nl/min flow rate on an Easy nLC1200 UPLC (ThermoScientific, Waltham, MA, USA) and the eluted peptides were examined on an Orbitrap Fusion mass spectrometer (ThermoScientific, Waltham, MA, USA). Data-dependent MS/MS scans of the 14 most abundant ions were recorded (Orbitrap analyser resolution: 60,000, AGC target: 4.0e5, collision-induced dissociation fragmentation in linear ion trap with 35% normalized collision energy, AGC target: 2.0e3, dynamic exclusion 45 s). Protein identification was done with MaxQuant 1.6.2.10 software⁷⁷ searching against the Human SwissProt database (release: 2020.02, 20,394 sequence entries). The mass tolerance for parent ion was 20 ppm and for fragment ions 0.5 Da. The minimum peptide length was set to 7. Cys carbamidomethylation along with Met oxidation and N-terminal acetylation were set as variable modifications. Maximum two missed cleavage sites were allowed. Those proteins were considered, where at least two peptides identified with 1% FDR were present.

Sample preparation for CUT&RUN MS measurements

HeLa cells suspended in cell culture medium were mixed with equal volume of 1% LMP agarose diluted in PBS. Agarose blocks were prepared where each blocks contained 90 μ l of agarose/cell suspension with 2×10^6 cells. 5 blocks were used for each sample (sample 1: no ZAbA + pAG-MNase activated, sample 2: ZAbA + pAG-MNase not activated, sample 3: ZAbA + pAG-MNase activated). Following ZAbA or ZAbB labeling, anti-rabbit IgG was added as a secondary antibody to improve yield, where indicated (see Suppl. Table 4). Blocks were washed 3 times in 25 ml PBS for 10 min. Permeabilization of cells was performed in 25 ml ice cold lysis buffer (0.4% (v/v) Triton X-100, 300 mM NaCl, 1 mM EDTA, 10 mM Tris-HCl, pH 8.0) for 30 min, followed by treatment with 25 ml ice cold 1% (v/v) Triton X-100 dissolved in PBS/EDTA, for 30 min. Blocks were washed 4 times in 25 ml ice cold CUT&RUN Wash (designated CR Wash)/EDTA (20 mM HEPES, 150 mM NaCl, 0.5 mM spermidine and 5 mM EDTA) for 10 min. Using 5 blocks/sample, samples 2 and 3 were labeled with ZAbA at 4°C , overnight at a titer of 1:800 in 2.4 ml CR Wash/EDTA. After labeling, the blocks were washed 4 times in 10 ml ice cold CR Wash buffer (without EDTA) for 30 min and incubated with 10^{-3} U/ml

pAG-MNase in 10 ml CR Wash buffer for 2 h on ice. After digestion, MNase was washed out by 10 ml ice cold CR Wash buffer 4 times for 30 min on ice. Chromatin bound MNase was activated by 5 ml ice cold CR Wash buffer supplemented with 2 mM CaCl_2 for 30 min on ice. MNase digestion was stopped by adding 250 μ l of 0.5 M EDTA and the blocks were further incubated at 37°C , for 30 min. Eluted proteins were concentrated using a 10 K Amicon tube (Merck-Millipore, Darmstadt, Germany) and the buffer was changed to PBS. Proteins were eluted from the filter with 250 μ l 1 \times PBS and stored at -20°C for MS analyses. For details of sample processing, Orbitrap MS analyses and protein identification, see Supplementary Methods.

CUT&RUN sequencing

The agarose-embedded, permeabilized nuclei were treated with C9 or SCR at 1:100 dilution, at 4°C , overnight. The samples were sequentially incubated with the primary antibody and pAG-MNase and processed according to the CUT&RUN protocol⁷⁸ adapted to agarose embedding as described above. In the experiments where the LSC/MNase experimental conditions were used, the samples were first digested with MNase used at a concentration of 10^{-3} U/ml for 10 mins at 37°C min prior to antibody labeling and the subsequent steps involving the fusion protein. Polyclonal anti-H3K9me3 (ab8898; Abcam) and mouse monoclonal anti-H3K4me3 (ref. 74) were applied as above. After elution, the samples were digested with 20 μ g/ml Proteinase K (Thermo Fisher Scientific, Waltham, Massachusetts, USA) for 1 h at 55°C . Samples were subsequently purified by a PCR cleanup kit (Macherey-Nagel) and sent for sequencing. Using 5 ng DNA per sample, Libraries were prepared with Ovation Ultralow Library Systems V2 (Tecan) according to the manufacturer's instructions. The end-repairing step was followed by indexed adapter ligation and enrichment of adapter-ligated fragments by 10 PCR cycles. Fragment size distribution of the libraries was checked on BioAnalyser 2100 (Agilent). The means of the insert size distributions were mononucleosomal. Single read 75 bp sequencing reads were generated by NextSeq 500 sequencer (Illumina). Library preparation and sequencing were performed by the Genomic Medicine and Bioinformatics Core Facility of the University of Debrecen. For Bioinformatic analyses of CUT&RUN sequence data see Supplementary Methods.

Chromatin assembly and hydroxyapatite chromatography

Chromatin assembly reactions employing *Xenopus laevis* N1/N2- (H3, H4), mouse recombinant H2A.Z/H2B or H2A/H2B⁶, 900 ng pXbsF201 plasmid DNA and topoisomerase I were carried out, followed by supercoiling assays to ensure an equal number of nucleosomes between reconstitutes (a physiological spacing one nucleosome per 180 bp), as described previously⁷⁹. Assembled chromatin was applied to a hydroxyapatite column (Bio-Rad HTP) with 0.1 M NaCl, 0.1 M KPO_4 , pH 6.7 as described³⁹, and washed successively with 0.1 M NaCl, 0.2 M NaCl and 0.4 M NaCl in 0.1 M KPO_4 , pH 6.7. Histones were eluted by a stepwise increase in NaCl concentration from 0.6 to 1.2 M in 0.1 M KPO_4 , pH 6.7. The eluted fractions were loaded onto a 18% sodium dodecylsulfate-polyacrylamide gel and then stained with silver as described previously⁷⁹.

Fluorescence correlation spectroscopy (FCS). Sample preparation

Mononucleosomes were reconstituted by slow salt dialysis from recombinant histones and Cy5 labeled 170 bp long DNA fragments centered around the well positioning Widom sequence according to^{80,81}. The Cy5 label was used to determine the diffusion properties of the nucleosomes independently from the fluorescein labeled peptides. The quality of the reconstituted mononucleosomes was controlled by absorption spectroscopy revealing eventual aggregation and PAAGel electrophoresis allowing the quantification of unbound DNA in the

sample. Only preparations without detectable aggregation and with less than 5% of unbound DNA were used.

Commercial mononucleosomes containing H2A or H2A.Z histones (see experiments shown in Suppl. Fig. 18) were purchased from Tebubio (France) (cat. no. 16-0009 and 16-1014, respectively).

FCS measurements were carried out in 50 to 100 μ l volume on a sylanized Sensoplate plus 384-well plate (Greiner) at room temperature. 20 nM CF-labeled C9 peptide was either mixed with 100 nM reconstituted nucleosome or DNA or was measured alone in 5 mM or 700 mM NaCl TE (pH = 7.5). The mixture was allowed to equilibrate to RT for 0.5 h before measurement.

FCS measurements were performed on a Nikon A1 Eclipse Ti2 confocal laser-scanning microscope (Nikon, Tokyo, Japan), equipped with a Plan Apo 60 \times water immersion objective [NA = 1.27] and a PicoQuant - TCSPC-FCS upgrade kit (PicoQuant, Berlin, Germany). Fluorescence of the CF-tagged peptide was excited by the 488 nm laser line, for Cy5 a 635 nm laser line was used. Fluorescence of CF and Cy5 were filtered with 500–550 nm and 660–740 nm bandpass filters, and detected with single photon counting detectors (PicoQuant, Berlin, Germany). Measurements of 20 \times 10 second runs were taken with each sample. Fluorescence autocorrelation curves were calculated using the SymPhoTime64 software (PicoQuant, Berlin, Germany) at 200 time points from 300 ns to 1 s distributed on a quasi-logarithmic time scale. For fitting of the autocorrelation curves to obtain diffusion times and fraction of DNA- or nucleosome bounded C9-CF, see Supplementary Methods.

Since the diffusion coefficients (D) of the measured fluorescein and Cy5 samples depend on the viscosity of the environment (through the Stokes–Einstein equation), the calculated values of the lateral e^{-2} radius of the detection volumes are also affected by the refractive index of the solution⁸² likely in a wavelength-dependent manner. Therefore, the ratio of the lateral e^{-2} radii of the detection volumes with eq.3 was calculated for 5 mM as well as 700 mM NaCl.

For determining the fraction of unlabeled gDNA bounded C9-CF, τ_{D2} was not fixed in the fitting of the autocorrelation functions as it may have a broad size distribution. All correlation curves were fitted using the QuickFit 3.0 software.

Statistics and reproducibility

For statistical analyses, one-way ANOVA test was used. The p values are shown on the figures, the number of measurements/samples used for their calculation was as defined in the legends or provided in the respective source data file. No statistical method was used to pre-determine sample size. No data were excluded from the analyses.

Reporting summary

Further information on research design is available in the Nature Portfolio Reporting Summary linked to this article.

Data availability

The Whole Genome Sequencing datasets generated during the current study are available in the NCBI SRA repository, under the BioProject accession number [PRJNA853352](https://www.ncbi.nlm.nih.gov/bioproject/PRJNA853352), WGS BioSample accession numbers (SAMN29379375-78 and SAMN42397447-48). Microarray datasets were deposited into GEO database under accession number [GSE225680](https://www.ncbi.nlm.nih.gov/geo/query/acc.cgi?acc=GSE225680). The RNA-seq datasets generated during the current study are available in the NCBI SRA repository, under the BioProject accession number [PRJNA853352](https://www.ncbi.nlm.nih.gov/bioproject/PRJNA853352), BioSample accession numbers (SAMN32271841-49 and SAMN4239742244-46). The CUT&RUN data are available in the NCBI SRA repository, under the BioProject accession number [PRJNA853352](https://www.ncbi.nlm.nih.gov/bioproject/PRJNA853352), BioSample accession numbers (SAMN423974222-43). Mass spectrometric data are available via ProteomeXchange with identifier [PXID040998](https://www.ebi.ac.uk/psd/entry/PXD040998). All other datasets generated during and/or analyzed during the current study are available

from the corresponding author on reasonable request. Source data are provided with this paper.

References

- Kreienbaum, C., Paasche, L. W. & Hake, S. B. H2A.Z's 'social' network: functional partners of an enigmatic histone variant. *Trends Biochem. Sci.* **47**, 909–920 (2022).
- Colino-Sanguino, Y., Clark, S. J. & Valdes-Mora, F. The H2A.Z-nucleosome code in mammals: emerging functions. *Trends Genet.: TIG* **38**, 273–289 (2022).
- West, M. H. & Bonner, W. M. Histone 2A, a heteromorphous family of eight protein species. *Biochemistry* **19**, 3238–3245 (1980).
- Bonisch, C. & Hake, S. B. Histone H2A variants in nucleosomes and chromatin: more or less stable? *Nucleic Acids Res.* **40**, 10719–10741 (2012).
- Park, Y. J., Dyer, P. N., Tremethick, D. J. & Luger, K. A new fluorescence resonance energy transfer approach demonstrates that the histone variant H2AZ stabilizes the histone octamer within the nucleosome. *J. Biol. Chem.* **279**, 24274–24282 (2004).
- Fan, J. Y., Gordon, F., Luger, K., Hansen, J. C. & Tremethick, D. J. The essential histone variant H2A.Z regulates the equilibrium between different chromatin conformational states. *Nat. Struct. Biol.* **9**, 172–176 (2002).
- Thambirajah, A. A. et al. H2A.Z stabilizes chromatin in a way that is dependent on core histone acetylation. *J. Biol. Chem.* **281**, 20036–20044 (2006).
- Carruthers, L. M., Bednar, J., Woodcock, C. L. & Hansen, J. C. Linker histones stabilize the intrinsic salt-dependent folding of nucleosomal arrays: mechanistic ramifications for higher-order chromatin folding. *Biochemistry* **37**, 14776–14787 (1998).
- Zhou, J., Fan, J. Y., Rangasamy, D. & Tremethick, D. J. The nucleosome surface regulates chromatin compaction and couples it with transcriptional repression. *Nat. Struct. Mol. Biol.* **14**, 1070–1076 (2007).
- Mylonas, C., Lee, C., Auld, A. L., Cisse, I. I. & Boyer, L. A. A dual role for H2A.Z.1 in modulating the dynamics of RNA polymerase II initiation and elongation. *Nat. Struct. Mol. Biol.* **28**, 435–442 (2021).
- Chen, Z. et al. High-resolution and high-accuracy topographic and transcriptional maps of the nucleosome barrier. *Elife* **8**, e48281 (2019).
- Abbott, D. W., Ivanova, V. S., Wang, X., Bonner, W. M. & Ausio, J. Characterization of the stability and folding of H2A.Z chromatin particles: implications for transcriptional activation. *J. Biol. Chem.* **276**, 41945–41949 (2001).
- Henikoff, S. Labile H3.3+H2A.Z nucleosomes mark 'nucleosome-free regions'. *Nat. Genet.* **41**, 865–866 (2009).
- Jin, C. et al. H3.3/H2A.Z double variant-containing nucleosomes mark 'nucleosome-free regions' of active promoters and other regulatory regions. *Nat. Genet.* **41**, 941–945 (2009).
- Rudnizky, S. et al. H2A.Z controls the stability and mobility of nucleosomes to regulate expression of the LH genes. *Nat. Commun.* **7**, 12958 (2016).
- Hu, G. et al. H2A.Z facilitates access of active and repressive complexes to chromatin in embryonic stem cell self-renewal and differentiation. *Cell Stem Cell* **12**, 180–192 (2013).
- Hainer, S. J. & Fazzio, T. G. Regulation of Nucleosome Architecture and Factor Binding Revealed by Nuclease Footprinting of the ESC Genome. *Cell Rep.* **13**, 61–69 (2015).
- Murphy, K. E., Meng, F. W., Makowski, C. E. & Murphy, P. J. Genome-wide chromatin accessibility is restricted by ANP32E. *Nat. Commun.* **11**, 5063 (2020).
- Wen, Z., Zhang, L., Ruan, H. & Li, G. Histone variant H2A.Z regulates nucleosome unwrapping and CTCF binding in mouse ES cells. *Nucleic Acids Res.* **48**, 5939–5952 (2020).

20. Hoch, D. A., Stratton, J. J. & Gloss, L. M. Protein-protein Förster resonance energy transfer analysis of nucleosome core particles containing H2A and H2A.Z. *J. Mol. Biol.* **371**, 971–988 (2007).
21. Lewis, T. S., Sokolova, V., Jung, H., Ng, H. & Tan, D. Structural basis of chromatin regulation by histone variant H2A.Z. *Nucleic Acids Res.* **49**, 11379–11391 (2021).
22. Jung, H., Sokolova, V., Lee, G., Stevens, V. R. & Tan, D. Structural and biochemical characterization of the nucleosome containing variants H3.3 and H2A.Z. *Epigenomes* **8**, 21 (2024).
23. Cole, L. et al. Multiple roles of H2A.Z in regulating promoter chromatin architecture in human cells. *Nat. Commun.* **12**, 2524 (2021).
24. Sarcinella, E., Zuzarte, P. C., Lau, P. N., Draker, R. & Cheung, P. Monoubiquitylation of H2A.Z distinguishes its association with euchromatin or facultative heterochromatin. *Mol. Cell. Biol.* **27**, 6457–6468 (2007).
25. Ryan, D. P. & Tremethick, D. J. The interplay between H2A.Z and H3K9 methylation in regulating HP1 α binding to linker histone-containing chromatin. *Nucleic Acids Res.* **46**, 9353–9366 (2018).
26. Oberdoerffer, P. & Miller, K. M. Histone H2A variants: diversifying chromatin to ensure genome integrity. *Semin. Cell Dev. Biol.* **135**, 59–72 (2023).
27. Matsuda, R. et al. Identification and characterization of the two isoforms of the vertebrate H2A.Z histone variant. *Nucleic Acids Res.* **38**, 4263–4273 (2010).
28. Faast, R. et al. Histone variant H2A.Z is required for early mammalian development. *Curr. Biol.: CB* **11**, 1183–1187 (2001).
29. Greenberg, R. S., Long, H. K., Swigut, T. & Wysocka, J. Single amino acid change underlies distinct roles of H2A.Z subtypes in human syndrome. *Cell* **178**, 1421–1436.e1424 (2019).
30. Cheema, M. S. et al. Deciphering the enigma of the histone H2A.Z-1/H2A.Z-2 isoforms: novel insights and remaining questions. *Cells* **9**, 1167 (2020).
31. Sales-Gil, R. et al. Non-redundant functions of H2A.Z.1 and H2A.Z.2 in chromosome segregation and cell cycle progression. *EMBO Rep.* **22**, e52061 (2021).
32. Suto, R. K., Clarkson, M. J., Tremethick, D. J. & Luger, K. Crystal structure of a nucleosome core particle containing the variant histone H2A.Z. *Nat. Struct. Biol.* **7**, 1121–1124 (2000).
33. Bonisch, C. et al. H2A.Z.2.2 is an alternatively spliced histone H2A.Z variant that causes severe nucleosome destabilization. *Nucleic Acids Res.* **40**, 5951–5964 (2012).
34. Herchenrother, A., Wunderlich, T. M., Lan, J. & Hake, S. B. Spotlight on histone H2A variants: from B to X to Z. *Semin. Cell Dev. Biol.* **135**, 3–12 (2023).
35. Morioka, S. et al. High-speed atomic force microscopy reveals spontaneous nucleosome sliding of H2A.Z at the subsecond time scale. *Nano Lett.* **23**, 1696–1704 (2023).
36. Imre, L. et al. Nucleosome stability measured in situ by automated quantitative imaging. *Sci. Rep.* **7**, 12734 (2017).
37. Kusakabe, M. et al. Genetic complementation analysis showed distinct contributions of the N-terminal tail of H2A.Z to epigenetic regulations. *Genes Cells* **21**, 122–135 (2016).
38. Punzeler, S. et al. Multivalent binding of PWWP2A to H2A.Z regulates mitosis and neural crest differentiation. *EMBO J.* **36**, 2263–2279 (2017).
39. Li, W., Nagaraja, S., Delcuve, G. P., Hendzel, M. J. & Davie, J. R. Effects of histone acetylation, ubiquitination and variants on nucleosome stability. *Biochem. J.* **296**, 737–744 (1993).
40. Nmezi, B. et al. Concentric organization of A- and B-type lamins predicts their distinct roles in the spatial organization and stability of the nuclear lamina. *Proc. Natl Acad. Sci. USA* **116**, 4307–4315 (2019).
41. Cheema, M. S. & Ausio, J. Analytical ultracentrifuge analysis of nucleosomes assembled from recombinant, acid-extracted, HPLC-purified histones. *Methods Mol. Biol.* **1528**, 75–95 (2017).
42. Dryhurst, D. et al. Characterization of the histone H2A.Z-1 and H2A.Z-2 isoforms in vertebrates. *BMC Biol.* **7**, 86 (2009).
43. Fyodorov, D. V., Zhou, B. R., Skoultchi, A. I. & Bai, Y. Emerging roles of linker histones in regulating chromatin structure and function. *Nat. Rev. Mol. Cell Biol.* **19**, 192–206 (2018).
44. Douet, J. et al. MacroH2A histone variants maintain nuclear organization and heterochromatin architecture. *J. Cell Sci.* **130**, 1570–1582 (2017).
45. Skene, P. J. & Henikoff, S. An efficient targeted nuclease strategy for high-resolution mapping of DNA binding sites. *Elife* **6**, (2017).
46. Zhou, M. et al. Structural basis of nucleosome dynamics modulation by histone variants H2A.B and H2A.Z.2. *EMBO J.* **40**, e105907 (2021).
47. Gursoy-Yuzugullu, O., Ayrapetov, M. K. & Price, B. D. Histone chaperone Anp32e removes H2A.Z from DNA double-strand breaks and promotes nucleosome reorganization and DNA repair. *Proc. Natl Acad. Sci. USA* **112**, 7507–7512 (2015).
48. Mieczkowski, J. et al. MNase titration reveals differences between nucleosome occupancy and chromatin accessibility. *Nat. Commun.* **7**, 11485 (2016).
49. Chereji, R. V., Bryson, T. D. & Henikoff, S. Quantitative MNase-seq accurately maps nucleosome occupancy levels. *Genome Biol.* **20**, 198 (2019).
50. Becker, J. S. et al. Genomic and proteomic resolution of heterochromatin and its restriction of alternate fate genes. *Mol. Cell* **68**, 1023–1037.e1015 (2017).
51. Mazouchi, A., Liu, B., Bahram, A. & Gradinaru, C. C. On the performance of bioanalytical fluorescence correlation spectroscopy measurements in a multiparameter photon-counting microscope. *Anal. Chim. Acta* **688**, 61–69 (2011).
52. Gansen, A. et al. High precision FRET studies reveal reversible transitions in nucleosomes between microseconds and minutes. *Nat. Commun.* **9**, 4628 (2018).
53. Vardabasso, C. et al. Histone variant H2A.Z.2 mediates proliferation and drug sensitivity of malignant melanoma. *Mol. Cell* **59**, 75–88 (2015).
54. Saeed, S. et al. Chromatin accessibility, p300, and histone acetylation define PML-RAR α and AML1-ETO binding sites in acute myeloid leukemia. *Blood* **120**, 3058–3068 (2012).
55. Achinger-Kawecka, J. et al. Epigenetic reprogramming at estrogen-receptor binding sites alters 3D chromatin landscape in endocrine-resistant breast cancer. *Nat. Commun.* **11**, 320 (2020).
56. Oomen, M. E., Hansen, A. S., Liu, Y., Darzacq, X. & Dekker, J. CTCF sites display cell cycle-dependent dynamics in factor binding and nucleosome positioning. *Genome Res.* **29**, 236–249 (2019).
57. Sevilla, A. & Binda, O. Post-translational modifications of the histone variant H2AZ. *Stem Cell Res.* **12**, 289–295 (2014).
58. Colino-Sanguino, Y. et al. A read/write mechanism connects p300 bromodomain function to H2A.Z acetylation. *iScience* **21**, 773–788 (2019).
59. Giaimo, B. D., Ferrante, F., Herchenrother, A., Hake, S. B. & Borggrete, T. The histone variant H2A.Z in gene regulation. *Epigenetics Chromatin* **12**, 37 (2019).
60. Foster, E. R. & Downs, J. A. Methylation of H3 K4 and K79 is not strictly dependent on H2B K123 ubiquitylation. *J. Cell Biol.* **184**, 631–638 (2009).
61. Li, S., Wei, T. & Panchenko, A. R. Histone variant H2A.Z modulates nucleosome dynamics to promote DNA accessibility. *Nat. Commun.* **14**, 769 (2023).
62. Arya, G. & Schlick, T. A tale of tails: how histone tails mediate chromatin compaction in different salt and linker histone environments. *J. Phys. Chem. A* **113**, 4045–4059 (2009).
63. Flaus, A. Principles and practice of nucleosome positioning in vitro. *Front. Life Sci.* **5**, 27–25 (2011).

64. Pilotto, S. et al. Interplay among nucleosomal DNA, histone tails, and corepressor CoREST underlies LSD1-mediated H3 demethylation. *Proc. Natl Acad. Sci. USA* **112**, 2752–2757 (2015).
65. Luzhetskaya, O. P., Sedykh, S. E. & Nevinsky, G. A. How human H1 histone recognizes DNA. *Molecules* **25**, 4556 (2020).
66. Bosire, R. et al. Intercalation of small molecules into DNA in chromatin is primarily controlled by superhelical constraint. *PLoS ONE* **14**, e0224936 (2019).
67. Wang, A. Y., Aristizabal, M. J., Ryan, C., Krogan, N. J. & Kobor, M. S. Key functional regions in the histone variant H2A.Z C-terminal docking domain. *Mol. Cell. Biol.* **31**, 3871–3884 (2011).
68. Lee, S. K. & Wang, W. Roles of topoisomerases in heterochromatin, aging, and diseases. *Genes* **10**, 884 (2019).
69. Holmquist, G., Gray, M., Porter, T. & Jordan, J. Characterization of Giemsa dark- and light-band DNA. *Cell* **31**, 121–129 (1982).
70. Long, H. et al. H2A.Z facilitates licensing and activation of early replication origins. *Nature* **577**, 576–581 (2020).
71. Saitoh, Y. & Laemmli, U. K. Metaphase chromosome structure: bands arise from a differential folding path of the highly AT-rich scaffold. *Cell* **76**, 609–622 (1994).
72. Dijkwel, Y., Hart-Smith, G., Kurscheid, S. & Tremethick, D. J. ANP32e binds histone H2A.Z in a cell cycle-dependent manner and regulates its protein stability in the cytoplasm. *Mol. Cell. Biol.* **44**, 72–85 (2024).
73. Kimura, H. & Cook, P. R. Kinetics of core histones in living human cells: little exchange of H3 and H4 and some rapid exchange of H2B. *J. cell Biol.* **153**, 1341–1353 (2001).
74. Kimura, H., Hayashi-Takanaka, Y., Goto, Y., Takizawa, N. & Nozaki, N. The organization of histone H3 modifications as revealed by a panel of specific monoclonal antibodies. *Cell Struct. Funct.* **33**, 61–73 (2008).
75. Hayashi-Takanaka, Y. et al. Tracking epigenetic histone modifications in single cells using Fab-based live endogenous modification labeling. *Nucleic Acids Res.* **39**, 6475–6488 (2011).
76. Afgan, E. et al. The Galaxy platform for accessible, reproducible and collaborative biomedical analyses: 2018 update. *Nucleic Acids Res.* **46**, W537–W544 (2018).
77. Cox, J. & Mann, M. MaxQuant enables high peptide identification rates, individualized p.p.b.-range mass accuracies and proteome-wide protein quantification. *Nat. Biotechnol.* **26**, 1367–1372 (2008).
78. Meers, M. P., Bryson, T. D., Henikoff, J. G. & Henikoff, S. Improved CUT&RUN chromatin profiling tools. *Elife* **8**, e46314 (2019).
79. Tremethick, D. J. High mobility group proteins 14 and 17 can space nucleosomal particles deficient in histones H2A and H2B creating a template that is transcriptionally active. *J. Biol. Chem.* **269**, 28436–28442 (1994).
80. Toth, K., Brun, N. & Langowski, J. Chromatin compaction at the mononucleosome level. *Biochemistry* **45**, 1591–1598 (2006).
81. Gansen, A. et al. Nucleosome disassembly intermediates characterized by single-molecule FRET. *Proc. Natl Acad. Sci. USA* **106**, 15308–15313 (2009).
82. Enderlein, J., Gregor, I., Patra, D., Dertinger, T. & Kaupp, U. B. Performance of fluorescence correlation spectroscopy for measuring diffusion and concentration. *ChemPhysChem* **6**, 2324–2336 (2005).
- Nagy for technical help. Microscopy measurements were carried out at the Debrecen sub-Node of the Cellular Imaging Hungary Euro-BioImaging Node. Mass spectrometry analysis was carried out at the BMBI Proteomics Core Facility, Department of Biochemistry and Molecular Biology, University of Debrecen. Next-generation sequencing analysis was performed at the Genomic Medicine and Bioinformatics Core Facility, Department of Biochemistry and Molecular Biology, Faculty of Medicine, University of Debrecen, Debrecen, Hungary. The authors thank Mr. Soma Godó (UNICAM Ltd., Budapest, Hungary) for loaning the STEDYCON microscope. The authors acknowledge the support of the Freiburg Galaxy Team, Bioinformatics, University of Freiburg (Germany) funded by the Collaborative Research Centre 992 Medical Epigenetics (DFG grant SFB 992/1 2012) and the German Federal Ministry of Education and Research BMBF grant O31 A538A de.NBI-RBC. G.Sz. received funding from GINOP-2.3.2-15-2016-00044, GINOP-2.3.3-15-2016-00020, Hungarian National Science and Research Foundation OTKA K138524, K128770 (<https://nkfih.gov.hu/funding/otka>), COST EuroCellNet CA15214 and CA18127 (<https://www.eurocellnet.eu>); G.V. from OTKA NN129371 and ANN135107. The Orbitrap Fusion mass spectrometer was provided by GINOP-2.3.3-15-2016-00020 for the Proteomics Core Facility of Debrecen University. Part of the mass spectrometric analyses was supported by the following grants: the Economic Development and Innovation Operative Programmes GINOP-2.3.2-15-2016-00001 and GINOP-2.3.2-15-2016-00020, the ELKH Cloud for housing the Protein Prospector server at Szeged. The Hungarian Centre of Excellence for Molecular Medicine has received funding from the European Union's Horizon 2020 research and innovation program under grant agreement no. 739593. S.P. was supported by TKP2021-NKTA-34. R.B. was supported by Stipendium Hungaricum awarded by the Tempus Public Foundation (<https://tka.hu/english>), E.F.N. was supported by the Richter Gedeon Talentum Fund. The funders had no role in study design, data collection and analysis, decision to publish, or preparation of the manuscript. J.A. research on this topic was supported by a Canadian Institutes of Health (CIHR) grant.

Author contributions

L.I.: cytotoxicity measurements together with E.F.N., LSC experiments, confocal microscopic studies, texture analyses, peptide treatment of live cells, sample preparation for MS and RNA sequencing, optimization of CUT&RUN together with P.N.; M.H.: conceptualization of the DT40 experiments; M.H. and M.K.: microarray data; R.B. and Á.C.: bacterial production of plasmids; P.N.: CHEF electrophoresis, analyses of microarray data provided by M.H., bioinformatics analyses of sequencing data, preparation of reconstituted nucleosomes, doing the FCS measurements and data analyses together with G.Mo.; E.H.: Western blot analyses; Z.B.: advice on LSC; G.Sz.: conceptualization of the experiments, evaluation of data and writing of manuscript together with L.I.; G.Me. supervised peptide synthesis conducted by KNE; J.A.: advice and editing of the manuscript, M.T. developed the inducible GFP-H2A.Z system and provided advice regarding the CUT&RUN experiments; C.P.: provided shRNA and advice regarding H2A.Z silencing; D.T.: contributed the hydroxyapatite elution data and edited the manuscript; E.C. and Z.D.: performed MS data analyses; I.B. conducted the titration experiments with cyclodextrins; M.B.: advice on melanoma cell lines; K.T. provided the constituents for and supervised the nucleosome reconstitution experiments, and also supervised the analyses of the FCS data; G.V. discussed the FCS data and edited the manuscript; S.P. and B.S. contributed to the bioinformatic analyses of the RNA-seq data.

Competing interests

The authors declare no competing interests.

Acknowledgements

The authors thank Cyclolab Hungary for providing cyclodextrins, Sandra B. Hake (Giessen, Germany) for the PWWP2A-GFP plasmid, Kerstin Bystricky (Toulouse, France) for the gift of anti-H2A.Z antibody ab4174, Zheng Zhou (Beijing, China) for explanations regarding their cryo-EM data on H2A.Z structure, Hiroshi Kimura (Tokyo, Japan) for valuable methodical advice and gift of antibodies, Adel Vezendine

Additional information

Supplementary information The online version contains supplementary material available at <https://doi.org/10.1038/s41467-024-53514-9>.

Correspondence and requests for materials should be addressed to Gábor Szabó.

Peer review information *Nature Communications* thanks the anonymous reviewer(s) for their contribution to the peer review of this work. A peer review file is available.

Reprints and permissions information is available at <http://www.nature.com/reprints>

Publisher's note Springer Nature remains neutral with regard to jurisdictional claims in published maps and institutional affiliations.

Open Access This article is licensed under a Creative Commons Attribution-NonCommercial-NoDerivatives 4.0 International License, which permits any non-commercial use, sharing, distribution and reproduction in any medium or format, as long as you give appropriate credit to the original author(s) and the source, provide a link to the Creative Commons licence, and indicate if you modified the licensed material. You do not have permission under this licence to share adapted material derived from this article or parts of it. The images or other third party material in this article are included in the article's Creative Commons licence, unless indicated otherwise in a credit line to the material. If material is not included in the article's Creative Commons licence and your intended use is not permitted by statutory regulation or exceeds the permitted use, you will need to obtain permission directly from the copyright holder. To view a copy of this licence, visit <http://creativecommons.org/licenses/by-nc-nd/4.0/>.

© The Author(s) 2024